Article

Massive multiplexing of spatially resolved single neuron projections with axonal BARseq

Li Yuan [1], Xiaoyin Chen [1,2], Huiqing Zhan [1], Gilbert L. Henry[1] & Anthony M. Zador [1]✉

Neurons in the cortex are heterogeneous, sending diverse axonal projections to multiple brain regions. Unraveling the logic of these projections requires single-neuron resolution. Although a growing number of techniques have enabled high-throughput reconstruction, these techniques are typically limited to dozens or at most hundreds of neurons per brain, requiring that statistical analyses combine data from different specimens. Here we present axonal BARseq, a high-throughput approach based on reading out nucleic acid barcodes using in situ RNA sequencing, which enables analysis of even densely labeled neurons. As a proof of principle, we have mapped the long-range projections of >8000 primary auditory cortex neurons from a single male mouse. We identified major cell types based on projection targets and axonal trajectory. The large sample size enabled us to systematically quantify the projections of intratelencephalic (IT) neurons, and revealed that individual IT neurons project to different layers in an area-dependent fashion. Axonal BARseq is a powerful technique for studying the heterogeneity of single neuronal projections at high throughput within individual brains.

The mouse brain contains over 70 million neurons[1], and the combined length of their axonal trees stretches thousands of kilometers; in the human brain, there are orders of magnitude more. These axons form the scaffolding for neural circuits and hence for computation. Tracing these projections represents a formidable challenge. Traditionally, there are two main approaches. At one extreme, the projections of single neurons can be reconstructed at high resolution by labeling neurons one at a time, using e.g. the Golgi method or more modern sparse labeling based on viral delivery of fluorophores such as green fluorescent protein (GFP). Such single-neuron methods have undergone impressive advances in recent years, but even today allow the multiplexing of at most dozens of neurons from a single brain region[2–5]. Alternatively, the projections of major projection pathways can be assessed using bulk tracing methods. For example, a bolus of virus expressing a fluorophore can be injected into one brain area, enabling the major projections of neurons within that area to be visualized by microscopy. These techniques have been used to

systematically map the mesoscopic projections of the mouse brain[6–8]. Bulk methods reveal the projections of large populations of neurons, but at the cost of single-cell resolution. Thus, there is a tradeoff between throughput and single-cell resolution in traditional methods.

We have recently developed a novel suite of nucleic acid barcode-based tracing techniques, which provide a third alternative. The first-generation method for exploiting barcodes in the context of circuit mapping was Multiplexed Analysis of Projections by Sequencing (MAPseq)[9]. MAPseq can reliably and simultaneously map the projections of hundreds of thousands of individual neurons in a single experiment. MAPseq uniquely labels individual neurons by introducing random RNA sequences ("barcodes") via infection with a barcoded viral library. These random barcodes fill the cells and are co-expressed with a protein that has been engineered to bind to the barcode and drag it to distant axonal terminals. The pool of unique barcode identifiers is effectively infinite; even a 30 nucleotide (nt)-sequence has a potential diversity of $4^{30} \approx 10^{18}$ barcodes, far surpassing

the ~10^8 neurons in the mouse brain. This high diversity implies that most neurons are uniquely labeled. The barcode RNA can then be extracted from the axons in an area of interest to determine which neurons project there; the number of molecules with a specific barcode sequence collected from a region is used as a proxy for the strength of the projection (i.e., axonal volume) of that particular barcoded neuron, in much the same way that GFP intensity is used as a proxy for projection strength in conventional bulk injections[9]. Because high-throughput sequencing can quickly and inexpensively distinguish these barcodes, MAPseq can uncover the projections of hundreds of thousands of individual neurons in parallel within a single brain[10,11]. The throughput of MAPseq for assessing single neuron projection patterns in a single brain is currently unmatched by any other approach.

MAPseq was the first approach to exploit barcoding for neuronal mapping. However, because it relies on bulk sequencing of homogenized tissue, its spatial resolution is determined by the precision of dissection. To achieve higher resolution, we developed BARseq (Barcoded Anatomy Resolved by Sequencing), the next generation of sequencing-based tracing[12,13]. BARseq relies on in situ sequencing. Unlike conventional in situ hybridization, which uses a complementary probe to detect a specific RNA molecule in the cell, in situ sequencing obtains the exact sequence of each RNA target. This is a key difference, as the RNA barcode in any given cell is unique, unknown and highly diverse, making it very challenging to design probes in sufficient numbers for the desired targets. In contrast, in situ sequencing makes it straightforward to discriminate an almost infinite number of sequences. Combining BARseq-based sequencing of somatic barcodes and endogenous gene expression with MAPseq-based dissection and sequencing of barcodes in the axons allows us to associate the projection patterns of individual neurons with soma locations in a highly multiplexed manner[12,13]. However, because spatial resolution in MAPseq is limited by the dissection of brain areas prior to bulk sequencing, axonal projection patterns in this MAPseq/BARseq combined approach can only be crudely resolved. MAPseq and BARseq have been repeatedly validated using multiple methods in a wide range of brain areas[8–21]. In particular, we demonstrated that barcode transport is uniform over long distances (>10 mm)[8–21].

We therefore set out to increase the spatial resolution with which highly multiplexed axonal trajectories can be resolved using in situ sequencing. To achieve this, we developed a method, "axonal BARseq," for sequencing individual axonal "rolling circle colonies", or "rolonies", in situ. Axonal BARseq allows much finer resolution of the spatial organization of axonal projections than can be achieved with MAPseq. Using this approach, we identify the projections of thousands of individual axons projecting from a single localized injection in a single mouse, increasing throughput beyond current methods and eliminating the need to register injections across samples. Axonal BARseq has the potential to scale up to multiple injection sites and reveal projections from multiple sites, raising the possibility of sampling brain-wide projections from multiple neuronal populations at single-cell resolution.

Results

Here we describe axonal BARseq, a highly multiplexed method for reconstructing axonal trajectories. We first describe the optimizations necessary to achieve single molecule sequencing of barcodes in axons. Next, we demonstrate its application to determine axonal projections from auditory cortex. We confirm that the single-neuron projection patterns obtained by this method are consistent with previous single-neuron approaches. We then show that the high resolution and multiplexing of axonal BARseq reveals the statistical structure of single neuron projections to different laminae in different areas.

Optimizing BARseq to achieve axonal resolution

We have previously demonstrated in situ read-out of barcodes expressed in somata[12,13]. This is a much easier problem than the present challenge of reading out single axonal barcodes, because there are several orders of magnitude more barcodes in somata (10^3–10^4)[9]. We, therefore, sought to maximize the sensitivity of in situ read-out of barcodes to achieve high-efficiency single-barcode readout of barcodes transported millimeters or centimeters from their soma of origin.

To increase the sensitivity of in situ sequencing of axonal barcodes, we modified the sequencing protocols originally developed for barcodes in somata[12,22]. The basic in situ sequencing protocol consists of (1) injection with a Sindbis virus engineered to express a diverse barcode library; (2) tissue preparation 24–48 h after infection; (3) preparation of rolonies (nanoballs of DNA generated by reverse transcription of the RNA barcode, followed by gap-filling padlock-extension, ligation, and rolling circle amplification) in thin brain slices; (4) in situ sequencing by synthesis using standard Illumina reagents: sequential four-color imaging of each base in the barcode of each rolony (see *Methods*; Fig. 1A, Supplementary Fig. 1A). We optimized the reverse transcriptase used and the gap-filling procedure (Supplementary Fig. 1B–D), which increased the sensitivity of barcode detection to an efficiency of 20.2% compared to RNA in situ hybridization (Supplementary Fig. 1E–F). In addition, we engineered a Sindbis virus using a second-generation carrier protein (VAMP2nλ), which carried barcodes more efficiently than our previously described carrier protein (see *Methods*).

A further challenge of single-barcode axonal sequencing is to achieve the requisite sensitivity and accuracy during successive rounds of in situ sequencing. The signal from a single axonal rolony is not as bright as that from larger somata because somata contain many copies of the same barcode (Fig. 1B, C). In addition, alignment of single rolonies across successive rounds of imaging poses additional challenges compared with alignment of somata. Overcoming these challenges required considerable modifications and optimization (see *Methods*, Supplementary Fig. 2–4).

Axonal BARseq of projections from auditory cortex

To assess the utility of these optimizations, we used axonal BARseq to reconstruct projections from mouse primary auditory cortex. Two days following unilateral viral injection, we performed 17 cycles of sequencing of coronal sections centered +/- 1 mm around the injection site (108 serial 20 μm sections). These sections contained many of the main projection targets of the auditory cortex, including most of the contra- and ipsilateral auditory cortices (AudC, AudI), contra and ipsilateral visual cortex (VisC, VisI), ipsilateral thalamus (Thal), part of the ipsilateral striatum (Str) and part of the ipsilateral superior colliculus (SupCol) (Fig. 1D, E, Supplementary Fig. 5A, SupTable 1). A total of 8620 unique axonal barcodes (obtained from 492,950 sequenced rolonies) were used for analysis, with a median of 40 rolonies per barcode. About half (3698/8620) of the reliably detected axonal barcodes could be associated with somata whose position could be confidently determined (Fig. 1F, Supplementary Fig. 5B); the remaining barcodes could not be precisely localized due to various experimental and analytical challenges (see *Methods*). However, for most of the subsequent analyses (with the exception of Fig. 5 and partial Supplementary Fig. 9), we used the entire set of axonal barcodes as the analyses do not require information about soma depth. Rolonies close to somata at the injection site were excluded (see *Methods*). Barcode statistics are summarized in Supplementary Fig. 5C–G; for details of manual validation of sensitivity and accuracy see *Methods*.

In conventional neuroanatomical single-neuron reconstructions, tracing requires that neuronal processes be filled with markers such as GFP or dyes, enabling visualization of axons as continuous structures. Disruption of this continuity due to errors in sample preparation or imaging can disrupt tracing and lead to catastrophic errors in reconstruction, potentially causing misattribution of an axon to the incorrect soma of origin. By contrast, because BARseq assigns axons to their
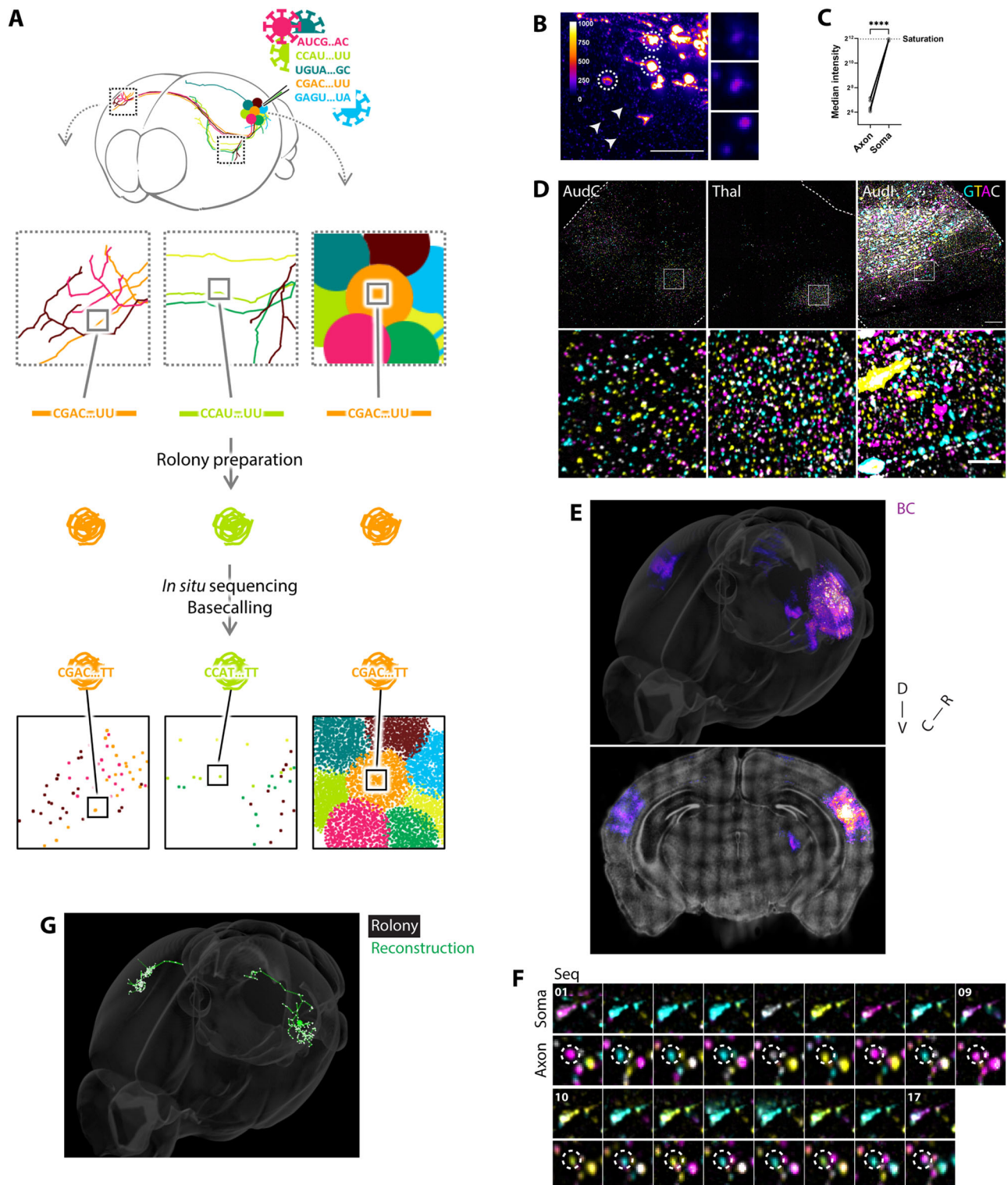
Fig. 1 | Overview of axonal BARseq. A Workflow. The brain is injected with barcoded viral library. After 24–48 h of expression, during which RNA barcodes are transported to axon terminals, where they are amplified into rolonies and sequenced. **B, C** Single rolonies in axons have significantly weaker signals compared to somatic rolonies. **B** Representative image of somatic and axonal rolonies; dotted circle: somatic rolonies; arrow: axonal rolonies, with zoom-in views shown on the right; rolony intensity is color coded. Scale bar: 100 μm. **C** Quantification of intensity between axonal and somatic rolonies. Due to the large intensity difference between somatic and axonal rolonies, proper exposure for axonal rolonies often results in saturation of somatic rolonies. Paired t-test, two-tailed, p-value < 0.0001. **D** Representative images of axonal and somatic rolonies in AudC/I and ipsilateral thalamus. Images are from the first cycle of in situ sequencing. Similar results are observed across sections of the same brain regions. Dotted line, anatomical boundaries. Scale bar: top, 100 μm; bottom, 25 μm. **E** Registered barcode signals in CCFv3. Top, data in 3D model. Gray, brain outline. Bottom, coronal view of 25 μm of the sample. Gray, DAPI. **F** Representative images of in situ sequencing soma and a single axonal rolony with the same barcode. Soma ROI, 30.25 μm × 30.25 μm from injection site; axonal rolony ROI, 14.85 μm × 14.85 μm from ipsilateral thalamus. In total, 17 sequencing cycles are shown. **G** An example of tracing tracks for a single barcoded neuron reconstructed by connecting rolonies. Rolony location is indicated in white; soma location is indicated as a large green dot in ipsilateral cortex. AudC/I, contra/ipsilateral auditory cortex; Thal, thalamus; BC, barcode; D, dorsal; V, ventral; C, caudal; R, rostral; Seq, sequencing cycle.
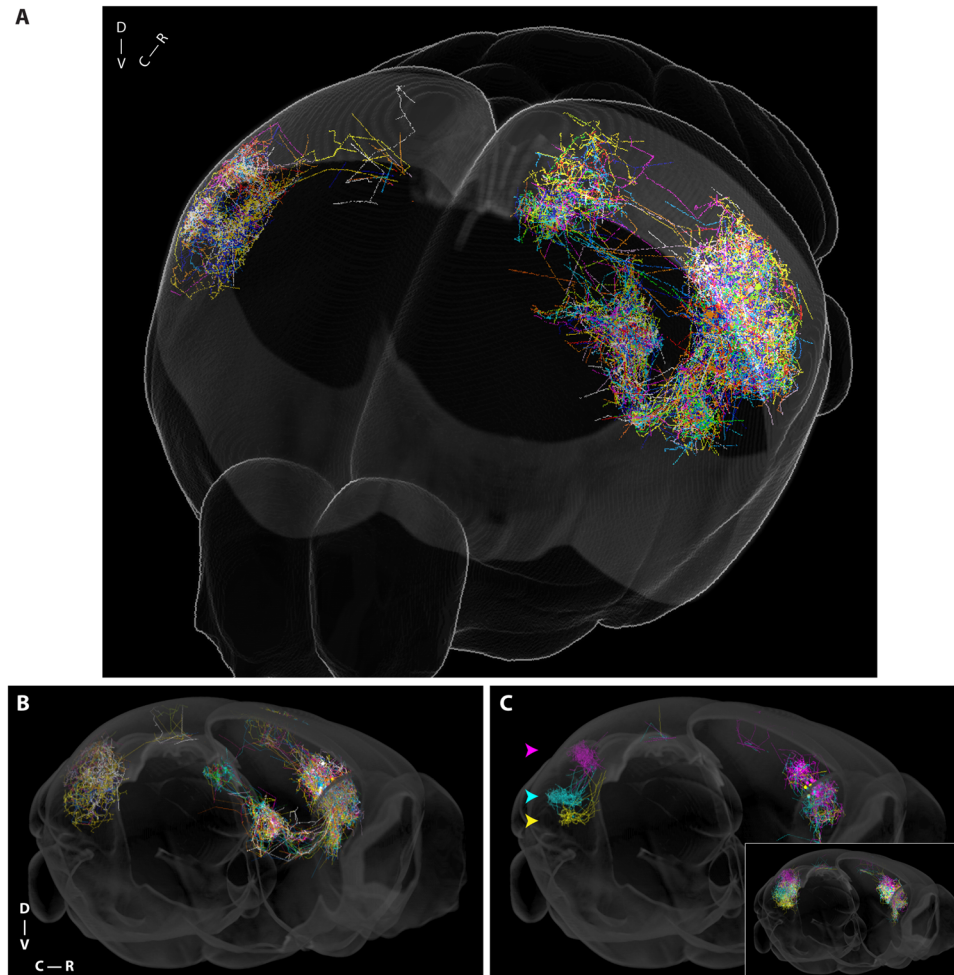
Fig. 2 | Axonal barcodes can be used to reconstruct axonal projection in anterograde and simulated retrograde tracing. A, **B** Single-cell reconstruction from 100 barcoded neurons, 25 from each major cell type (ET, CT, ITc, ITi) as described below. Somas (colors randomly assigned) are indicated by large dots in the left hemisphere. Not all tracts were imaged. Note that these reconstructions are approximate because many fine processes are not detected, and that only the 2 mm *shaded region* was reconstructed (the entire brain is included for reference). The reconstructions are used for visualization purposes only; all quantifications rely directly on the rolonies themselves rather than the reconstructions. **C** Identifying cells with focal projections to the same locations by simulated retrograde tracing. Cells from three simulated retrograde injections are indicated by arrows in the right hemisphere. (*inset*) For each simulated injection, 25 neurons were randomly selected and plotted, regardless of whether their projections were focal or broad.

soma of origin on the basis of their barcode sequences, assignments can be accurate even when barcodes are sparse. Errors in appropriate attribution of a barcode (e.g. due to sequencing errors) are rare and, importantly, are not catastrophic because they are independent, i.e. a given error affects only a single rolony.

We identified 8620 axonal barcodes outside the injection site, including ipsi- and contralateral cortex (CtxI and CtxC), thalamus, caudal striatum, and superior colliculus (Supplementary Fig. 6A). For visualization purposes, it can be convenient to connect barcode rolonies to generate images that are similar to conventional neuroanatomical reconstructions. An example of such a connect-the-dots visualization, with straight lines linking nearby barcodes with the same sequence (see *Methods*), is shown in Fig. 1G. In cases where the inter-barcode distance is large, this reconstruction is only an approximation, since axons can sometimes take tortuous paths, which may not be fully captured by this approximation. However, these reconstructions are used for display purposes only; all quantifications rely directly on the rolonies themselves rather than the reconstructions. Figure 2A, B shows the trajectories of 100 neurons (out of 8620), color-coded for display purposes (see 3D rotation animation, Supplementary Movie 1).

The large number of barcoded single neurons allowed us to identify subpopulations of neurons with distinct projection patterns. Figure 2C (*inset*) shows a simulated contralateral retrograde injection of three colors. Among these neurons, subsets could be identified that projected very narrowly to specific patches (Fig. 2C). The identification of such subpopulations is facilitated by the high density of labeling obtained with axonal BARseq and would have been difficult to identify using conventional anterograde or retrograde methods. Analyses such as these highlight how the high degree of multiplexing (within a single sample) inherent in axonal BARseq enables identification of potentially interesting subpopulations.

Axonal BARseq can identify cell types based on projection trajectory

Following previous analyses of auditory cortex[12] and other cortical structures[23], we manually clustered barcoded neurons into major cell types (Fig. 3A, Supplementary Fig. 6A, B). The top-level partition, between corticofugal (CF) and intratelencephalic (IT) classes, was based on the presence of subcortical projections descending below striatum, including the ipsilateral thalamus and the superior colliculus. IT cells were further divided into ITi and ITc, based on whether they
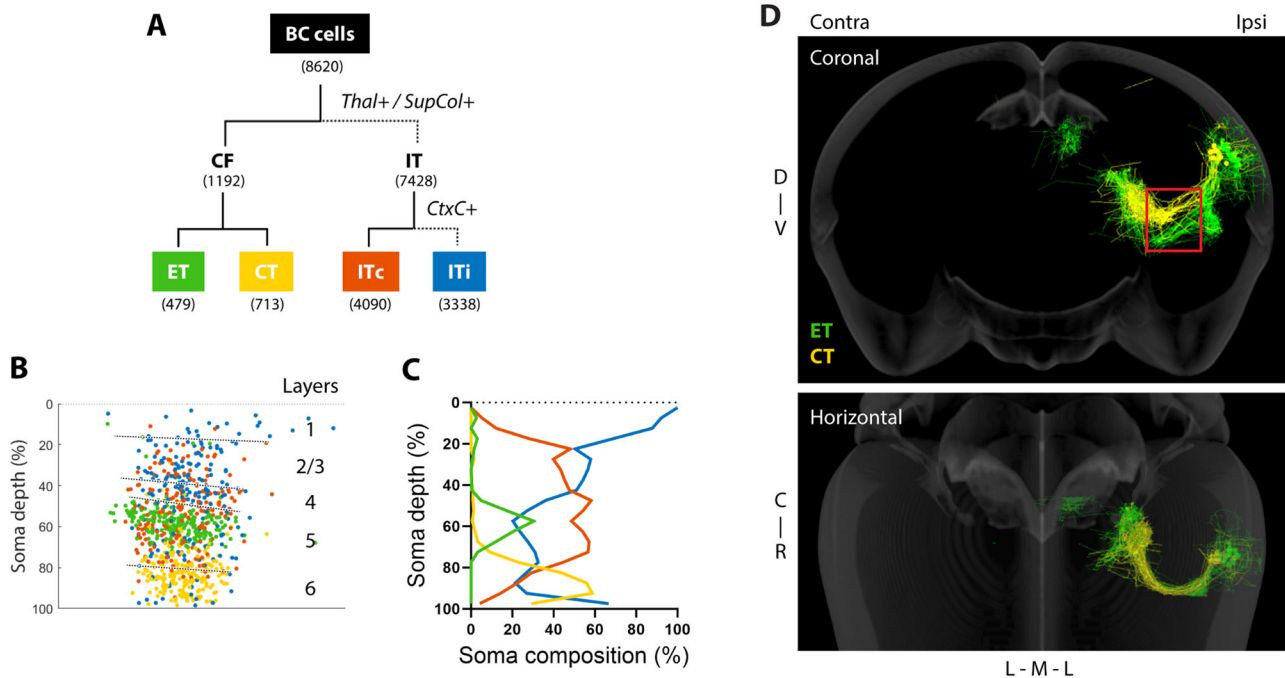
Fig. 3 | Cells can be divided into major cell types using projection targets and axonal trajectory. A Barcoded cells were divided into four cell types: ET, CT, ITc and ITi. Cells were divided into CF/IT using Thal/SupCol projection; IT cells were divided into ITi/ITc using contralateral cortical projection. SupCol was identified using the midbrain area in CCFv3. Solid line, with the specific projection; dotted line, without the projection. Numbers next to the group names indicate cell counts of the groups. **B, C** Soma depth of four cell types in the injection site. **B** Scatter plot of 200 randomly selected cells per group. Layer annotations are from CCFv3. **C** The distribution of the four cell types along depth. Cell types were color coded as in Fig. 3A. **D** Projection tracts of CT and ET neurons consistent with spatial features of both cell types, 60 randomly selected neurons per type. Red box, region of interest for CT/ET grouping. Coronal view, top; horizontal view, bottom. CT/ET rolonies with region boundaries were shown in Supplementary Fig. 7F, G. SupCol, superior colliculus; CtxC/I, contra/ipsilateral cortex; CF, corticofugal; IT, intratelencephalic; ET, extratelencephalic; CT, corticothalamic; L, lateral; M, medial.

had projections to the contralateral cortex. Barcoded somata were distributed across laminae and particularly enriched in mid layers (Supplementary Fig. 6C). Consistent with previous studies, CF somata were found predominantly in layer 5 (L5) and layer 6 (L6), whereas ITi and ITc somata were distributed across layers (Fig. 3B, C, Supplementary Fig. 6D)[2,7,8,12]. Thus, the projection patterns observed with axonal BARseq recapitulate those observed with conventional methods and with previous studies using BARseq.

CF neurons are divided into two major types[23]: extratelencephalic (ET, also known as pyramidal tract/PT neurons) and corticothalamic (CT). ET and CT neurons are distinct in the laminar positions of their somata[23], axonal trajectory[6], gene expression[24,25], and projection targets. ET neurons from the auditory cortex project to both the tectum[12] and higher order thalamic nuclei, including lateral posterior nucleus (LP), posterior limiting nucleus (POL), posterior intralaminar thalamic nucleus (PIL) and peripeduncular nucleus (PP)[7,26]. In contrast, CT neurons do not project to the tectum and mainly project to medial geniculate body (MG) in the thalamus[7,27]. In previous work[12] we distinguished ET neurons from CT neurons by the fact that only ET neurons project to the tectum. In the current experiment, however, we did not sample the entire tectum, and thus could not distinguish these two populations of neurons by the presence or absence of tectal projections. Instead, we exploited the high spatial resolution of axonal BARseq to partition neurons based on axonal trajectory.

Figure 3D shows representative axonal trajectories to the thalamus of CF neurons. One group follows a dorsal route and travels through the reticular nucleus, whereas the second follows a ventral route. These two routes are consistent with the two axonal trajectories of CT and ET neurons, respectively (Supplementary Fig. 7A–D)[6,28]. We further combined axonal BARseq with immunohistochemistry to distinguish projections to different thalamic nuclei (Supplementary Fig. 7F, G. Consistent with the hypothesis that these two trajectories distinguish CT and ET neurons, neurons taking the dorsal route are concentrated in L5 (peak around 60% depth; Fig. 3B, C) and project to LP, POL, PIL/PP (Fig. 3D, Supplementary Fig. 7F, G). By contrast, neurons taking the ventral route are concentrated in L6 (peak around 90% depth; Fig. 3B, C) and project to the MG (Fig. 3D, Supplementary Fig. 7F, G). These results indicate that axonal BARseq can distinguish populations of projection neurons based on axonal trajectory.

Diversity of laminar terminations across areas
The cortex is organized hierarchically, with primary sensory areas like auditory cortex representing the lowest level of the hierarchy. Feedforward projections–those that go up the hierarchy–often terminate in layer 4 of cortex, whereas feedback projections go to lower layers. Recently, Harris et al. reported[7] that hierarchical position alone does not explain all of the connections made by a given area, and suggested that more complex models would be needed, with labels richer than just feedforward and feedback. However, the results of Harris and colleagues were based primarily on labeling of populations of neurons, leaving open the possibility that feedforward and feedback projections could be well-defined at the level of single neurons. We therefore studied the characteristics of areal and laminar projections across a large population of single neurons.

For the purposes of this analysis, we divided the cortex into four target areas: LatI, MedI, MedC and LatC (ipsilateral-lateral, ipsilateral-medial, contralateral-medial, contralateral-lateral, Fig. 4A). LatI/C mainly consists of auditory areas, whereas MedI/C mainly consists of higher-order visual areas (also called parietal associative areas)[29,30]. The majority of IT neurons from primary auditory cortex projected only to lateral (82.7%) areas, while almost no neurons (0.26%) projected to medial areas alone, and 17.1% projected to both. Thus, almost
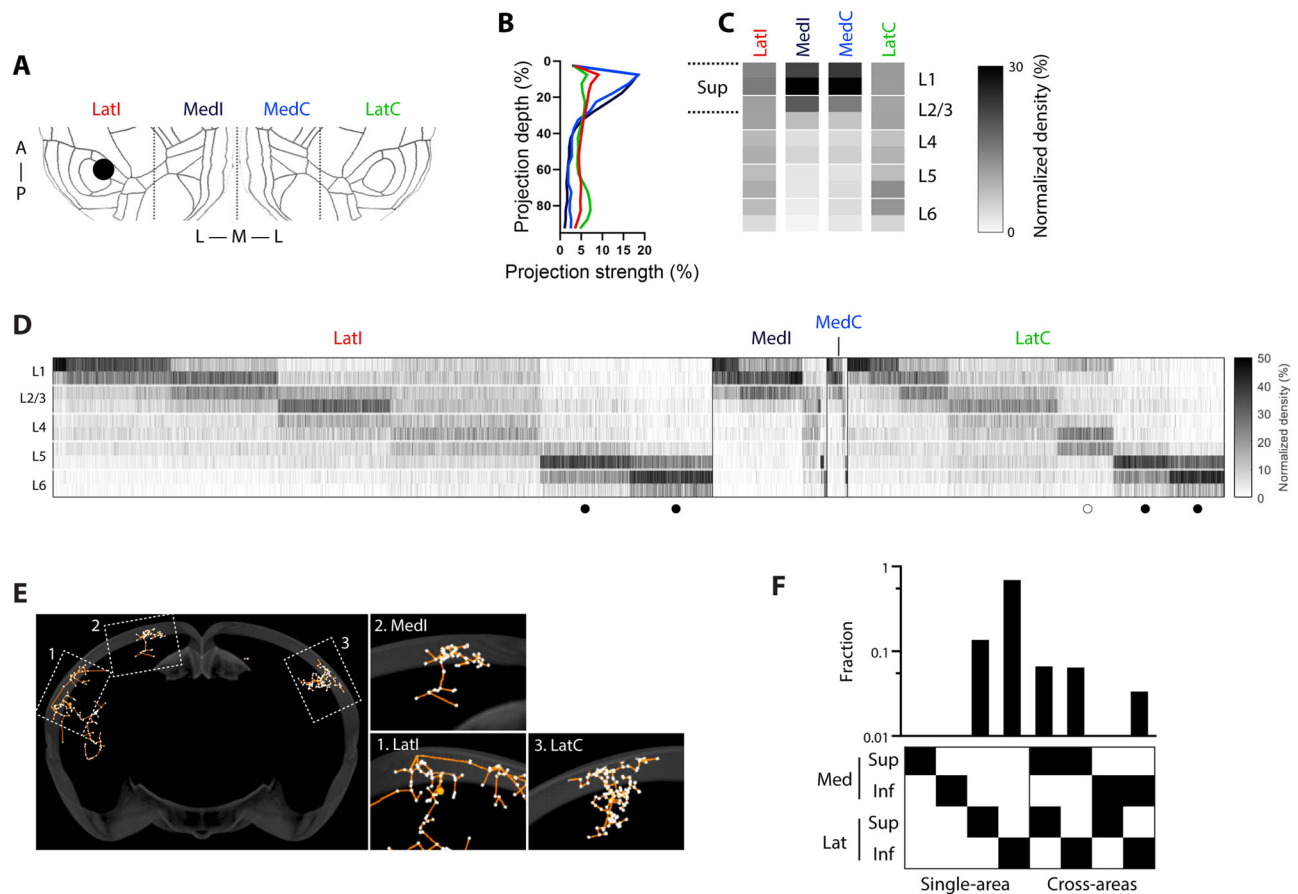
Fig. 4 | IT projections demonstrate diversity across cortical areas, within individual areas, and across different areas within single cells. A Division of cortex into medial and lateral targets on flatmap: LatI, MedI, MedC, and LatC. Black disk, injection site. The cortical flatmap was generated from CCFv3[30] (see *Methods*). **B, C** Different laminar patterns of bulk projections in medial and lateral cortical targets. **B** Frequency distribution of projection strength along projection depth. Bin size, 5% depth. **C** Heatmap of the normalized projection density in each layer. Each layer is divided into upper and lower halves. Superficial layer (Sup) refers to projections from L1 to upper L2/3. To calculate the normalized density, rolony counts were normalized to the layer thickness and the total rolony counts per column. Cell counts: LatI, 6,878; MedI, 1,196; MedC, 212; LatC, 3,931. **D** Distinct laminar patterns of single-cell projections in medial and lateral cortical targets. The heatmap illustrates the normalized projection density in each layer, with one cell per column. Laminar patterns were clustered using *k*-means. **E** Coronal view of representative single-cell reconstruction (orange) and axonal rolonies (white) of an IT neuron with multiple cortical targets. Soma, big orange dot in AudI. Zoom-in view: 1, LatI; 2, MedI; 3, LatC. **F** Sup/Inf projection probability depends on Lat/Med projection patterns. Within a given area, neurons are categorized based on their predominant projection type (x-axis), e,g, a neuron is classified as 'Sup' if > 50% of its projections are superficial; otherwise, it is classified as 'Inf'. Neurons that project only to a single area project only to Lat, and predominantly inferiorly, whereas neurons that project to both Lat and Med project with nearly equal probability to Sup and Inf. LatI/C, ipsi/contralateral lateral; MedI/C, ipsi/contralateral medial; A, anterior; P, posterior.

every neuron that targeted medial neurons also targeted lateral areas, but not vice versa, suggesting that information from neurons in the primary auditory cortex is obligatorily conveyed to primary and higher auditory areas (Lat), but only optionally to non-auditory areas (Med).

We next assessed laminar heterogeneity of projections to different cortical areas. The bulk-level laminar termination patterns of corticocortical projections are consistent with those observed in the Allen Mouse Brain Connectivity Atlas[6]: projections to medial areas were largely localized to superficial layers (layer 1 to upper layer 2/3), whereas those to lateral areas were distributed across layers (Fig. 4B, Supplementary Fig. 8A–C). Because projection density in medial areas decreased strongly within layer 2/3 in our data set, as well as in data from the Allen atlas, we defined the border between "superficial" and "inferior" projections at the mid-point of layer 2/3 (Fig. 4C, Supplementary Fig. 8D, E). Note that this border, defined by axonal projection density, does not correspond to the conventional boundaries used to demarcate the borders between layers 1-6 defined by somatic properties.

There are several ways in which the bulk-level projection pattern (superficial targets for medial areas and mixed superficial and inferior targets in lateral areas) could arise. At one extreme, the population could be homogeneous: every neuron could project to every layer in every area. At the other extreme, the population could consist of highly specialized neurons, with each neuron projecting to only one layer and only one area. Between these two extremes, there could be subpopulations with specific patterns of projections. To disambiguate these possibilities, we examined the laminar terminations between medial and lateral areas at single-cell resolution. The neurons targeting medial areas projected mainly to superficial layers (as expected from the bulk data) and formed a relatively homogeneous population (Fig. 4D, Supplementary Fig. 8F). By contrast, single-neuron projection patterns in lateral areas were heterogenous, consisting of several diverse subpopulations. Although superficial projections are traditionally thought to be feedback projections, we consider those to the medial areas as feedforward based on the following considerations: Harris et al. suggest[7] that these are feedforward rather than feedback; moreover, projections from the auditory cortex to higher-order areas are, by definition, feedforward.

In Fig. 4D, the diverse projection patterns are clustered for visualization purposes. Some neurons mainly project to superficial

layers, representing a feedforward pattern; some mainly target deep inferior layers (Fig. 4D, *dot-labeled*), suggesting a feedback pattern. Additionally, there are neurons that project more diffusely across various layers, constituting an apparent mix of feedforward and feedback projections. An example neuron with projections mainly to superficial layers in MedI, but with diffuse projections to both superficial and inferior layers in LatI and LatC, is shown in Fig. 4E. Thus, it appears that the observed laminar projection patterns fall between the two extremes, with subpopulations showing specific patterns of projections. Our observations reinforce, at the single neuron level, the conclusions of Harris et al.[7], who found a mix of feedforward and feedback projections in Cre-defined neuronal populations. These results suggest a need for more nuanced categories beyond the simple "feedforward" and "feedback" dichotomy.

Additionally we asked about the consistency of a laminar projection pattern at the single neuron level across cortical areas, using the superficial pattern as a representative example for this analysis. For neurons that project solely to a lateral target, the probability of projecting predominantly to the inferior layers (83.5%) is much higher than the probability of projecting to superficial layers (16.5%) (Fig. 4F, Supplementary Fig. 8G, H). However, for neurons that also project to a medial target, those same lateral projection probabilities nearly equalize (57.2% vs. 42.8%, respectively). Thus, the subpopulation of neurons that project to both medial and lateral areas are predisposed, but not determined, to project to superficial targets in both areas.

Diversity of projections within an area

We next examined the relationship between soma laminar position and the laminar structure of axonal projections to different cortical targets. We divided Lat-projecting cells into three groups based on soma layer (Fig. 5A): upper (layer 1 to layer 2/3, in red), middle (layer 4 to upper layer 5, in orange), and deep (lower layer 5 to layer 6, in blue). Using these divisions, we found that at the bulk level, the deep (*blue*) somata mainly projected to deep layers (lower layer 5 to layer 6 as defined previously), whereas the upper and middle somata preferentially projected to upper-middle layers of their targets (Fig. 5B, Supplementary Fig. 9A, B). Notably, the upper border of deep projections is located around mid-layer 5 (Figs. 4D and 5E)[31], which does not conform to the laminar boundaries.

We then compared the organization of these projections to LatI/C at the single-cell level. Three example neurons are illustrated in Fig. 5C, D. In these examples, and across the population (Fig. 5E), projections from upper and middle somata to both areas (LatI, LatC) were largely enriched in upper-middle layers. The tendency of deep somata to project to deep targets is also reflected in Fig. 4D: 77.7% of deep-projection clusters (also see Supplementary Fig. 9C, *dot-labeled*) arose from deep somata. Moreover, we observed a marked correlation between the depth of a deep somata and the proportion of deep-projections (Supplementary Fig. 9D). Thus, the most superficial of the "deep" somata had more upper/middle-layer projections, and the proportion of upper/middle-layer projection gradually decreased with somatic depth[12]. The correlation between soma depth and projection target was further validated by a *post hoc* analysis of injection variability across wild-type mice in the Allen Mouse Brain Connectivity Atlas (Supplementary Fig. 10). Also, the subset of callosal projections that terminate around the boundary between layer 4 and 5, and layer 1 in Fig. 4D, largely originated from middle-layer somata (84.8%, Supplementary Fig. 9C, *circle-labelled*). Similar projection patterns were observed from the middle somata (layer 4 and 5 IT Cre lines; Supplementary Fig. 9E, F), underscoring the consistency of laminar projection patterns between traditional Cre-based bulk tracing and axonal BARseq. Furthermore, we found that upper somata were less likely to project to ipsilateral striatum, and middle somata were more likely to project to Med cortex compared to the other two groups (Fig. 5F–H, Supplementary Fig. 9G, I; see also 7,8).

We next analyzed the fanout pattern of axonal projections within a target area. In LatC, upper somata tended to focus their axonal terminations in a small area (Fig. 5C, D, red neuron), whereas deep somata tended to project more diffusely (Fig. 5C, D, blue neuron), with middle somata exhibiting an intermediate pattern (e.g. two foci; see Fig. 5C, D, orange neuron). These observations are summarized across the population in Fig. 5I (see also Supplementary Fig. 9J–N, Supplementary Fig. 11). Taken together, axonal BARseq resolved systematic differences in the projections of layer-defined subpopulations of IT neurons in the laminar patterns of axon termination, their projection targets, and the projection patterns within a target.

Discussion

We have described axonal BARseq, a highly multiplexed method for mapping neuronal projections with single-cell resolution. A key advantage of axonal BARseq over conventional optical methods is the large number of projections that can be mapped in a single brain. As a proof-of-principle, we used axonal BARseq to map the projections of more than 8000 neurons from primary auditory cortex of a single mouse. Axonal BARseq represents an advance in spatial resolution over first-generation BARseq, which relied on bulk sequencing to read out projection barcodes. We used this large data set to systematically quantify the heterogeneity of auditory cortical projections to multiple targets. Additionally, we showed that axonal BARseq can be combined with routine immunohistology (Supplementary Fig. 7G).

The central challenge in multiplexed mapping of axonal projections is that the axons are densely packed and tangled together. When the distance between two axons approaches or falls below the limit of optical microscopy, the fidelity with which they can be distinguished using classical methods decreases. The greater the number of labeled axons, the greater the probability that two axons will be indistinguishable, and thus the greater the probability of error. Tracing errors are catastrophic because the error implies that an axon will be misattributed to the incorrect soma of origin. These challenges are particularly acute when tracing axons over long distances, because axons often travel in bundles. Such considerations limit the number of labeled axons that can be optically reconstructed within a single specimen.

Axonal BARseq provides an alternative anatomical approach that eliminates the need to follow the entire axonal trajectory. Instead, barcodes provide a direct means of associating the axon with its parent soma. Errors in appropriate attribution of a barcode (e.g. due to sequencing errors) are rare and, importantly, are not catastrophic because they are limited to a single rolony. Moreover, projections to distant targets can be assessed even without the need to trace the entire axonal path from soma to target. This enables efficient mapping of projections to multiple target areas, even if the targets are widely separated in space. The use of Sindbis virus for neural barcoding has been validated across various studies employing diverse methodologies[8–10,12,15,19–21]. In particular, barcode transport is uniform even for long axons, as initially demonstrated in the locus coeruleus[9], For a more complete discussion of the possible confounds due to viral toxicity, co-infections, degenerate barcode libraries, and other potential sources of error, please refer to Kebschull et al. and Chen et al.[9,12].

The high throughput of axonal BARseq is useful for at least four reasons. First, high throughput allows for statistical analyses using large numbers of single neurons, which has the potential to reveal statistical structure that is not evident with smaller sample sizes. Second, the fact that the samples come from a single animal is useful when individual animals are rare or valuable, such as for nonhuman primates, non-canonical model systems, transgenic animals, or animals that have been subjected to specific treatments or manipulations. Third, axonal BARseq allows for dense mapping of projections within a single brain, obviating the need to register all results to a single reference atlas. Avoiding registration eliminates the errors that arise
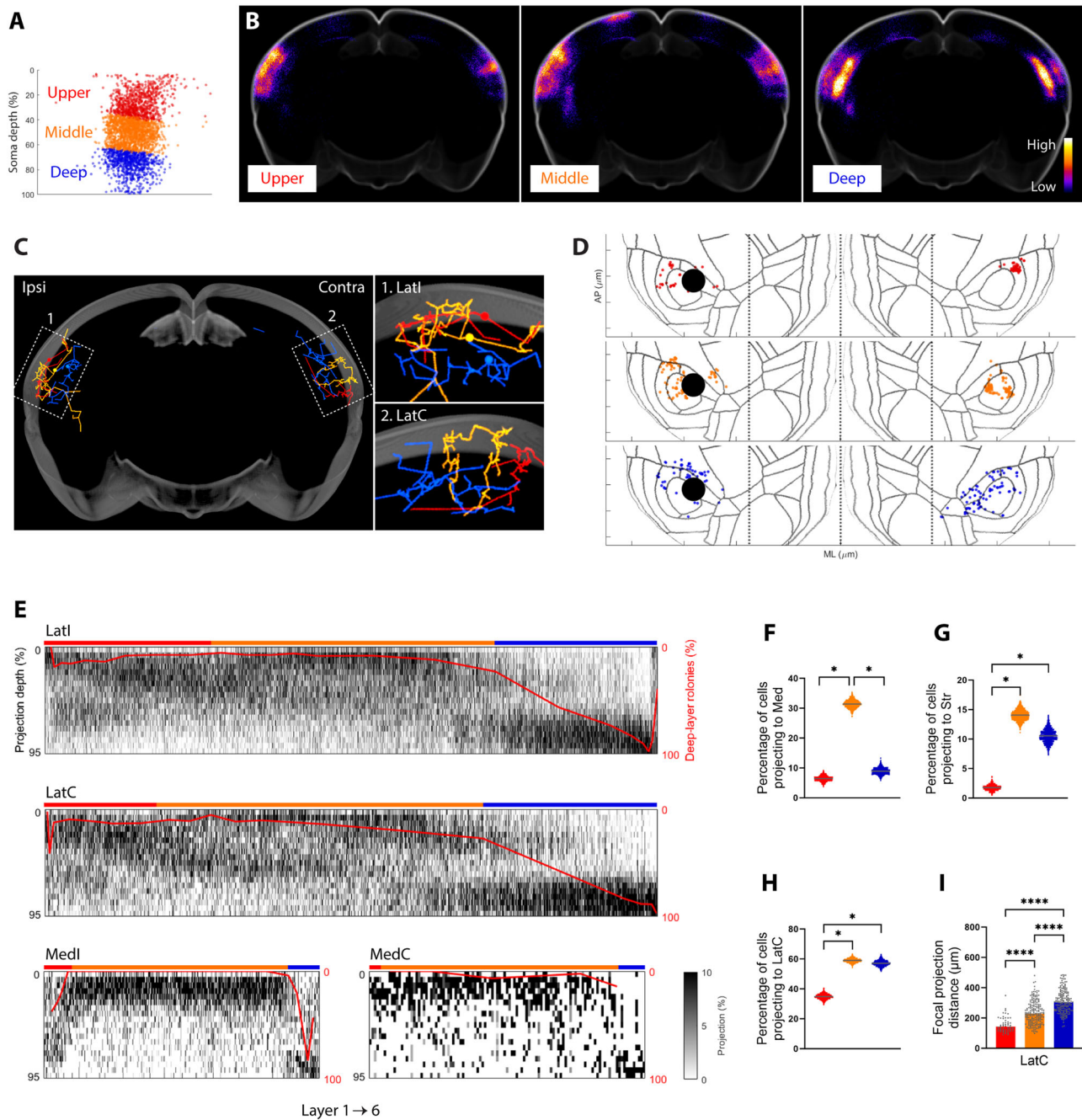
Fig. 5 | Diversity in laminar terminations, morphology, and targets across three groups of IT cells. **A** Lat-projecting IT cells were divided into three groups using soma layers: upper, layer 1 and 2/3; middle, layer 4 to upper layer 5; deep, lower layer 5 and layer 6. Cell counts: upper, 853; middle, 1450; deep, 806. **B** The three groups have different rolony distribution patterns at bulk level. 806 barcodes per group were randomly selected for display purposes. Images shown are sum projections of coronal views. **C** Representative single-cell reconstructions of three biLat cells. One cell for each group. Zoom-in panel: 1, LatI; 2, LatC. Soma, big dots in AudI. **D** Rolony location of individual neurons in Fig. 5C on cortical flatmap. Dotted lines, Med-Lat boundaries. Ticks on x/y-axis, 2000/1000 μm; x/y-axis ratio, 1:1. **E** At the single-cell level, deep somata mainly project to deep layers, while upper and middle somata preferentially project to upper-middle layers. Heatmap, frequency distribution of rolony along depth; bin size, 5% depth; one cell per column. Cells

were sorted by layer location of somata (x-axis). Red line: percentage of deep-projection (lower layer 5 and layer 6). Cells were binned into 5% bins using soma depth, and median percentage of deep-projection was calculated per bin. Cell counts: LatI, 3,012; MedI, 525; MedC, 113; LatC, 1,612. **F–H** Middle somata have a higher percentage of cells that project to the medial cortical areas (**F**), while upper somata have a lower percentage of cells projecting to the ipsilateral striatum and contralateral lateral areas (**G, H**). Gray line, median; bootstrapping was performed for each group (2,000 iterations); *, significant difference with no overlap CI. **I** Upper/middle somata have more focal projection in LatC compared to deep somata. The focal projection distances were computed based on distances between rolonies (see *Methods*). Bar graph, median; dots, individual cells. Cell counts: upper 54; middle, 186; deep, 178. Kruskal-Wallis test, Dunn's test for multiple comparisons, *p*-value < 0.0001. AP, anterior-posterior axis; ML, medial-lateral axis.

from comparing across brains. Moreover, registration implicitly assumes that all brains are the same, whereas in some cases idiosyncratic differences between brains may be important. Finally, axonal BARseq can be combined with in situ gene sequencing (BARseq2)[13],

allowing high-throughput correlation of gene expression with projection pattern. These advantages make axonal BARseq uniquely useful for certain applications, such as studying the relative topography of projections.

Here, we used axonal BARseq to simultaneously trace different cell types within a single wild-type animal. By tracing the subcortical projecting cell types, ET and CT, we directly observed the differences between them, including the laminar distributions of their somata and their projection patterns in the thalamus (Fig. 3D, Supplementary Fig. 7F, G). We identified hundreds of IT cells projecting to multiple cortical targets, and were able to quantify the extent to which single neuron projections to different brain areas terminated in different laminae (Fig. 4D). We also found that IT cells can have focal or sparse patterns in their contralateral projections, with sparse projections originating from deep-layer cells and targeting deep layers (Fig. 5D and I). Focal projections originated from upper-middle layer cells with a different laminar distribution. Our results demonstrate that axonal BARseq can recapitulates previously observed differences between cell types and is highly effective in making novel discoveries in heterogeneous cell populations.

Limitations and future developments

Axonal BARseq has several limitations compared with other methods. First, like conventional GFP-based tracing approaches, axonal BARseq reveals only axonal projections but not synaptic connections. To achieve synaptic resolution requires electron microscopy or visualizing synaptic markers using super-resolution microscopy. Second, because rolonies can be spaced as far as tens of microns apart, reconstructed axons might lack anatomical detail. This means that branch points or even entire branches may be missed, which can affect the accuracy of the reconstructed neuronal projections. Although the neuroanatomical literature has traditionally placed a high premium on reconstructing the finest processes with high fidelity, for many applications the increased throughput–thousands of neurons per sample–may represent a useful tradeoff. For example, if the main interest is in the laminar distribution of axonal innervation (Fig. 4D and Fig. 5E), the fact that not all fine axonal processes are recovered may represent an acceptable compromise. It may also be possible to increase the density of axonal rolonies and thus the fidelity of reconstruction by improving the delivery of barcodes to axons (e.g. with a better carrier protein) and by refining the protocols for rolony recovery. Additionally, it might be possible to combine axonal BARseq with either classic fluorophore-based tracing or brainbow[32]. Finally, in the current work we did not attempt to resolve local axons near the injection site because of limitations of the current algorithms for automated base-calling of rolonies. However, newer algorithms may make it possible to resolve rolonies at high density. Due to the nature of in situ sample preparation and sequencing, such as limited permeability for reagents and potential interference from biomolecules in the tissue, axonal BARseq may exhibit a higher false negative rate compared to MAPseq.

There are several potential avenues for improving upon the current axonal BARseq method. First, axonal BARseq could be combined with conventional GFP-based tracing techniques. By combining the higher resolution of conventional single neuron tracing–the ability to resolve even the finest axonal branches– with the higher throughput of axonal BARseq. Second, axonal BARseq can be combined with the expression of endogenous genes, which would enable us to correlate projection patterns with transcriptomically defined cell types, allowing a better understanding of the differences in projection patterns both among and within cell types. Finally, we expect that it will be possible to increase the number of cells that can be analyzed using axonal BARseq. In general, the number of cells recovered by BARseq is determined by the size of the injection. In this study we restricted our injection to a single site, labeling a relatively small number of neurons. However, in previous work[10] we have barcoded more than 100,000 neurons in a single brain, and there is no technical barrier to labeling comparable numbers of neurons for axonal BARseq in future studies. Furthermore, Sindbis virus can infect diverse species including

primates[14], so axonal BARseq could potentially be modified to map projections in many model systems, especially those in which conventional tracing-based approaches are impractical. Axonal BARseq thus has the potential to emerge as a powerful tool for massively multiplexed mapping of single neuron projections in diverse model systems.

Methods

Sindbis virus barcode library

The sindbis virus (SINV) barcode library used in this study was generated by the MAPseq core facility at Cold Spring Harbor Laboratory. The VAMP2nλ vector was derived from the MAPP-nλ SINV vector (Addgene #79785)[9] by replacing MAPP-nλ with VAMP2nλ. The VAMP2nλ consists of an nλ RNA binding domain, a V5-tag, and a mouse VAMP2 sequence. Oligos containing 30 nucleotide barcodes, including 28 random nucleotides and 2 fixed nucleotides, were synthesized by IDT. The barcoded virus library was produced as previously described[33]. Briefly, the digested oligos were inserted into SINV genomic vectors, transformed by electroporation for plasmid production. The plasmids were then linearized, and RNAs were in vitro transcribed using the mMES-SAGE SP6 kit. The SINV genomic and package RNAs (Addgene #72309) were transfected into BHK cells using Lipofectamine 2000. After two days of expression, the SINV supernatant was filtered and ultracentrifuged for virus purification. The virus pellets were resuspended in 1xPBS and stored at −80 °C. The VAMP2nλ SINV library exhibits a diversity of approximately 4 million barcodes, as determined by Illumina sequencing.

Animal processing and tissue preparation

All animal procedures were approved by the Institutional Animal Care and Use Committee at Cold Spring Harbor Laboratory (protocol 19-16-10-07-03-00-4). Mice were housed under a 12-hour dark/light cycle, at temperatures ranging from 21.1 to 23.3 °C, with 30–70% humidity. Experiments were performed on 7–10 week-old male C57BL/6 mice (Charles River). The VAMP2nλ SINV library was injected into the primary auditory cortex using the NanojectIII (Drummond) at the following coordinates: −2.5 mm AP, ± 4.2 mm ML, 0.9, 0.6, 0.3 mm depth, with a volume of 150 nL per depth. The mouse used for axonal BARseq was injected at −4.2 mm ML. After 2 days of expression, animals were anesthetized and perfused with 4% PFA in 1X PBS. The samples were post-fixed at 4 °C for a day and then transferred to sucrose gradients (10–15%, 20–22%, 30% sucrose in 1X PBS at 4 °C) and frozen in OCT. The brains were cryosectioned at 20 μm thickness, mounted onto glass slides using UV-solidified glue (Norland Optical Adhesive NOA81, 8–10 s UV) to minimize section distortion or detachment during high temperature and chemical treatments.

Rolony preparation

Before starting sample preparation, the sections were thawed and a hybridization chamber was placed on top. In the axonal rolony experiments, one section per chamber was utilized, while in the axonal BARseq experiment, two adjacent sections were used per chamber. To eliminate any residual fluids, chambers and samples were rinsed with water or reaction buffer before crucial reactions. For extended reactions or overnight reactions, humidified chambers were employed to prevent section dehydration. The catalog numbers and oligos utilized are listed in SupTable 2, respectively. The differences between this protocol and the BARseq protocol[12] are listed in SupTable 3.

Sample pretreatment. Samples were washed twice with 1% PBSTE (1XPBS with 1% Tween-20 and 5 mM EDTA) and incubated in 1% PBSTE at 65 °C for 8-9 min. Next, they were placed on ice for 2 min and washed twice with 1% PBSTE. The samples were then dehydrated in 50%, 70%, and 85% ethanol and incubated in 100% ethanol overnight at 4 °C. After two washes with 100% ethanol, the samples were washed

twice with water and 1% PBSTE to smooth the chamber. They were briefly washed in 4 mM HCl to adjust the pH for pepsin digestion and then digested with 0.1–0.2% pepsin (w/v) in 4 mM HCl with 1 μM XC1215 at pH ~ 3 at 33 °C for 30-40 min. It is important to note that the activity of the pepsin solution varies batch-to-batch and the activity of each batch was tested. Similarly, the pH of the solution was monitored as a low pH results in high nuclear background during in situ sequencing, while a more neutral pH leads to low pepsin activity. Finally, the duration of pepsin digestion was closely monitored, as over-digestion can cause tissue/rolony degradation/tearing or falling off, while insufficient digestion can lead to low permeability and low rolony density.

Reverse transcription. After digestion, samples were washed twice with 1% PBST and then washed in 1X SSIV (SuperScript IV) buffer containing 0.4 μg/μL BSA and 5 mM DTT for 5–15 min at room temperature. Reverse transcription was performed on the samples using 1 μM XC1215, 20 U/μL SSIV, 500 μM dNTP, 0.2 μg/μL BSA, 1 U/μL Ribo-Lock RNase Inhibitor, and 5 mM DTT in 1X SSIV buffer at 45 °C for approximately 4 h. Samples were then transferred to a new reaction mix and incubated overnight at 45 °C.

For the reagent comparison experiment (Supplementary Fig. 1B, C), samples treated with RA (RevertAid H minus reverse transcriptase) were washed in 1X RA buffers containing 0.4 μg/μL BSA for 5–15 min at room temperature. Reverse transcription was performed on the samples using 1 μM XC1125, 20 U/μL RA, 500 μM dNTP, 0.2 μg/μL BSA, and 1 U/μL RiboLock RNase Inhibitor in 1X RA buffer at 37 °C for approximately 4 h. The samples were then transferred to a new RA reaction mix and incubated overnight at 37 °C.

After reverse transcription, the samples were washed with 1X PBS and crosslinked with 25 mM BS(PEG)9 in 0.2% PBST for 30 min at room temperature. They were then washed with 0.2% PBST (0.2% Tween) and incubated in 2 mM lysine in 1X PBS for 30 min.

Gapfilling. After crosslinking, the samples were washed with 0.2% PBST twice and with water twice, and then gapfilled with 100 nM padlock probe LYO5, 0.5 U/μL Ampligase, 50 μM dNTP, 0.4 U/μL RNaseH, 50 mM KCl, 20% formamide, and 12.5 mU/μL Phusion in 1X Ampligase buffer at 37 °C for 30–40 min, and 45 °C for 45 min. To prevent Phusion from reacting with the padlock, the reaction mix was kept cold and Phusion was added immediately before the reaction. In the reagent comparison (Supplementary Fig. 1B, D), padlock probe LYO5 was replaced by XC1164.

Rolling circle amplification (RCA). After gapfilling, the samples were washed thoroughly with 0.2% PBST and rinsed with water. They were then incubated with RCA mix (1 U/μl EquiPhi29 polymerase, 0.25 mM dNTP, 120 μM aadUTP, 0.2 μg/μL BSA, and 1 mM DTT in 1X EquiPhi29 buffer) at 37 °C overnight. After incubation, the samples were washed with PBS once and crosslinked with 25 mM BS(PEG)9 in 0.2% PBST for 15 min at room temperature. They were then washed with 0.2% PBST twice and quenched with 1 M Tris pH 8.0 for 30 min. This RCA-crosslinking step was repeated two more times. After three rounds of RCA, the samples were crosslinked with 25 mM BS(PEG)9 in 0.2% PBST for 30 min at room temperature. They were then washed with 0.2% PBST twice and quenched with 1 M Tris pH 8.0 for 30 min.

Axonal barcode detection comparison
To measure the sensitivity of rolony preparation, we compared it to FISH, a standard method with high single-molecule sensitivity. In these experiments, rolonies were hybridized with fluorescence-conjugated probes. After rolony preparation, the samples were hybridized with 0.25 μM probe XC92 in 2X SSC, 10% formamide for 15–30 min at room temperature. Any excess probes were washed away three times with 2X SSC, 10% formamide, and three times with 0.2% PBST.

In the experiments used to compare rolony preparation and FISH, the FISH samples were pretreated in the same way as the rolony preparation samples. After digestion, they were washed, and FISH was performed using GFP probes and the RNAscope kit according to the manufacturer's protocol.

Quantification was performed using max-projected and stitched images. Similar regions of interest were manually selected in the AudI/AudC/Thal/VisI for each brain section, avoiding somatic rolonies. Rolony counts were measured using 'Find Maxima' with fixed prominence in Fiji, and density was calculated by dividing by the area size. Rolony densities were normalized to the density of the same region in neighboring SSIV + LYO5 samples. The median of the normalized density was calculated from 2–4 regions per section.

Interestingly, we found that a 2 nt length difference between padlock probes LYO5 and XC1164 significantly affected rolony signals. This may be because template length affects Phi29 efficiency during RCA[34]. While the modified protocol generated more axonal rolonies, it was less cost-effective for producing somatic rolonies. Therefore, for somatic barcode sequencing, the original BaristaSeq protocol[22] is sufficient due to the high abundance of somatic barcodes.

Axonal and somatic rolony comparison
Probe-hybridized samples in Supplementary Fig. 1E, F were used for comparison of axonal and somatic rolonies. For each brain section, 10–20 somatic areas were manually selected in AudI, and somatic rolony intensities were represented by the maximum intensity of each somatic area. In the same stitched images, 6-7 300 × 300 pixel ROIs were manually selected for axonal rolonies, avoiding somatic rolonies. Within each ROI, axonal rolonies were identified using 'Find Maxima' in Fiji, and axonal rolony intensities were represented by the intensity of the maxima. The median intensities of axonal and somatic rolonies were calculated for each section, with background subtraction.

In situ sequencing
Axonal BARseq samples were split into seven rounds of rolony preparation (SupTable 1). For each round, the samples were divided into two batches for in situ sequencing. After rolony preparation, the samples were incubated in 2X SSC, 80% formamide at 65 °C for 15 min. 2.5 μM sequencing primer LYO23 was hybridized to the rolonies in 2X SSC, 10% formamide for 15–30 min at room temperature. Any excess primers were washed away three times with 2X SSC, 10% formamide, and three times with 0.2% PBST. In situ sequencing was performed using the HiSeq Rapid SBS Kit v2 (Illumina). The reagents used in this process included the Universal Sequencing Buffer (USB), Cleavage Reagent Mix (CRM), Cleavage Wash Mix (CWM), Incorporation Master Mix (IMT), and Universal Scan Mix (USM). Before the first cycle, the samples were washed with USB at 60 °C for 4-5 min twice. Then, they were incubated with CRM at 60 °C for 5 min. The samples were washed three times with CWM, 1% TT (20 mM Tris pH 8.0, 1% Tween-20), and twice with PBS. Next, they were blocked with iodoacetamide (9.3 mg tablet in 2 mL 1XPBS) at 60 °C for 4-5 min and washed with 0.2% PBST three times. For each sequencing cycle, the samples were washed with USB at room temperature twice and incubated with IMT at 60 °C for 4 min. They were then washed with 1% TT with 5 mM EDTA once, and 1% TT at 60 °C for 4 min 3–5 times. The samples were incubated in USM and were ready for imaging. After imaging, the samples were washed with 1% TT three times and USB twice, incubated with CRM at 60 °C for 4 min, and washed with CWM. In the later sequencing cycles, the C-channel often had a high level of nonspecific background; additional 1% TT washes were included to decrease this background. In round 1 of this dataset, the samples did not receive CRM treatment before the iodoacetamide incubation prior to Seq01. Additionally, an extra iodoacetamide treatment was applied after the first CRM step following Seq01 imaging.

Immunohistochemistry

After the final sequencing cycle (Seq17), the samples were treated with CRM and CWM to remove any remaining sequencing signals. They were then blocked with 5% BSA in 1X PBS and incubated with a vGlut2 antibody (1:500) in 2% BSA in 1X PBS at 4 °C for 2 days. Following washes with 0.2% PBST, the samples were incubated with a secondary antibody (1:1,000) in 2% BSA for 2–4 h at room temperature. After additional washing, the samples were stained with DAPI and imaged using USM.

Microscopy

Images were obtained using a Nikon TE2000-E microscope equipped with an X-Light V2 spinning disk (Crest Optics), Prime 95B camera (Teledyne Photometrics), and LDI-7 laser diode illuminator (89North). A 20X Plan Apo objective (Nikon) was used for all experiments. It is important to note that factors such as optical distortion and uneven illumination in the microscope system can affect the sensitivity and accuracy of axonal BARseq. Images were acquired using μManager 1.4[35]. All images were taken as z-stacks with the following settings: 0.55 μm per pixel, 12-bit depth, a total of 17 stacks with 3 μm intervals, and 15% overlap for tiling. The lasers and filters used for each channel are listed in SupTable 2. Briefly, each nucleotide was imaged in a separate channel during sequencing. We found that maximum intensity projection preserved most of the signal while resulting in smaller file sizes and reduced computational demands during analysis. As a result, we converted the z-stacks to max projections.

Image processing and rolony identification

The general workflow for data acquisition and analysis is described in Supplementary Fig. 2A. In order to strike a balance between data output and imaging time, we opted to image selected target areas of auditory cortex. The target areas were initially identified through manual selection and subsequently registered to the corresponding coronal section obtained from the immunohistochemistry step to ensure accurate positioning. Due to the selection of target areas, processes outside these regions were not included in the current study.

The image processing workflow for in situ sequencing is described in Supplementary Fig. 2B. To reduce fixed pattern noise during in situ sequencing, we subtracted the 3rd lowest intensity plane of the z-stack from the maximum projection image. Local background subtraction was performed by taking advantage of the fact that pixels without a barcode have discontinuous intensity profile along the z-axis. This process effectively removed local signal distortions and backgrounds such as uneven illumination, nuclear, and tissue background (Supplementary Fig. 2C, D). However, while this method was effective for axonal rolonies in target areas, errors were encountered in pixels around the somata due to the high signal density and the aberrant intensity distribution along the z-axis compared to single rolonies. To correct for bleed-through, uneven channel intensity, and intensity decay across sequencing cycles, we based intensity corrections on local maxima for each experiment. To decrease variability between individual batches, we used z-scores for intensity correction. Rolonies were typically between 3–7 pixels in diameter on the maximum projection images. Therefore, we identified local maxima within a 5-pixel diameter range for each sequencing cycle. A local maximum was considered a rolony location if it met the following criteria: (1) in the z-stack, the slides with the highest intensity were neighboring slides (e.g. the 1st max intensity slide was next to the 2nd/3rd max intensity slides); (2) the channel with the local maximum had the highest intensity before and after image corrections; (3) the channel intensity passed the intensity ratio filter (i.e. 2nd max/1st max <0.95); (4) the max channel intensity passed a threshold. To improve the accuracy of matching rolonies during base-calling, we calculated the subpixel locations of local maxima using interpolation.

For immunohistochemical experiments, maximum projections of image tiles were stitched into whole coronal sections using phase correlation, with max projection in the overlapping region.

Tile alignment and stitching. The workflow for alignment and stitching is described in Supplementary Fig. 3A. The alignment process consists of two steps: (1) pre-alignment using stitched images; (2) point cloud registration for individual tiles.

During pre-alignment, tiles from the same image were initially stitched using imaging positions and then aligned across sequencing cycles using phase correlation. We used imaging position-based stitching to avoid errors from intensity-based algorithms. Additionally, stitched images were aligned to 1–3 sequencing cycles to minimize errors. After pre-alignment, rolony coordinates were aligned to the reference or neighboring sequencing cycles using a projective/affine transformation (Supplementary Fig. 3B). The transformation matrix between point clouds was calculated using a frequency-based algorithm. To reduce the impact of tissue distortion during sequencing, we used mid-sequencing cycles (Seq08/09) as reference cycles. Vis of section #76 was excluded during alignment.

For stitching, we combined and aligned the rolony coordinates from nearby tiles across sequencing cycles to the neighboring tiles. To minimize errors, we stitched tiles with a lower number of rolonies to tiles with a higher number of rolonies.

Rolony base-calling. Our rolony base-calling pipeline allowed for a degree of error during alignment. No non-linear transformations were performed during alignment. Base-calling was performed by matching nearby local maxima (dots) across sequencing cycles (Supplementary Fig. 3C). Dots were first given unique IDs in each sequencing cycle, and dots from later cycles were one-to-one matched to the closest available dots in the previous cycle within a 5-pixel range. The sequence of dots was then assembled, and the nucleotides associated with the dots were identified as the rolony barcode.

During sequencing, rolony signals may be lost, shifted, or near a strong nonspecific noise signal. To maximize continuity in the sequencing results, each rolony was matched to rolonies in three previous cycles. To assemble the sequence, matches were merged sequentially from a 0 to 3 cycle interval in ascending order (e.g., 3-4, 2-4, 1-4, 4-5, 3-5, 2-5, etc.). Non-base-called nucleotides were assigned to intervals when two matching cycles were not consecutive. If there was a disagreement between the current match and the existing sequence, the previous sequence was duplicated to include the new match (Supplementary Fig. 3C, blue). Barcodes with more than three continuous non-base-called nucleotides were discarded. However, due to the high density of signals and resulting higher error rate near the injection site, we excluded rolonies close to the soma (within 20 μm of ≥35 soma pixels in >2 cycles) from the analysis.

Soma base-calling. Since barcoded somata were larger in size compared to individual rolonies, we base-called somata using pixel location rather than local maxima. We identified the barcodes as the channels with the highest intensity across sequencing cycles using stitched images from the AudI. For technical reasons, the stitched images used for soma base-calling only included one tile for overlap areas.

During later sequencing cycles, we noticed that barcoded somata showed phasing signals, but single rolonies did not. This may be because somata contain a larger number of barcoded single-stranded DNA, and the protocol was not optimized for soma barcode sequencing. To digitally correct this, we subtracted the pixel intensity from the previous cycle (50% for maximum intensity and 100% for the rest), which improved the signal-to-noise ratio (Supplementary Fig. 3D).

Registering image to brain volume. We identified and imaged targeted brain regions separately for in situ sequencing. After alignment

and stitching, we registered the images to the whole coronal section using nuclear signals by phase correlation. We then aligned the coronal sections into a 3D volume using control point pairs. These point pairs were selected manually between nearby sections, and displacement fields were generated from polynomial2 and piecewise linear transformation within manually defined limits and corrections. One brain section (section #108) was excluded due to severe distortion.

Codebook and lookup table. We used the results of the in situ sequencing to construct a list (codebook) of infected barcodes. The two sources of barcode combinations are axons and soma. As this study focused primarily on axonal projections, we chose only axonal barcodes for our codebook (Supplementary Fig. 4A).

We tolerated 1-2 nt errors in our rolony base-calling protocol, since the base-calling process could have errors either due to single mutations during sample preparation or misalignments during analysis. This ensured the accuracy of the codebook/lookup table and minimized data loss.

As described above, the rolony base-calling procedure can base-call a rolony multiple times, resulting in a set of barcodes with and without errors. To construct our final codebook for this dataset, we made the following assumptions: (1) a true barcode can be found in multiple rolonies (≥3 rolonies); (2) a true barcode has a higher count than its erroneous versions; (3) there are no pairs of true barcodes within 1 Hamming distance (<0.1%, Supplementary Fig. 4B); (4) a true barcode consists of different nucleotides (<14 same nucleotides) and meets length limits (with ≥13 of 15 nucleotides base-called, ≤3 continuous non-base-called nucleotides). Based on these parameters, our codebook consisted of 13,919 barcodes.

Lookup tables were used to match individual axonal and somatic barcodes to the codebook. A Hamming distance of 2 was set as a cutoff to match axonal and somatic barcodes to the codebook barcodes. Barcodes that matched more than one codebook barcode within the minimum Hamming distance were discarded. During this process, non-base-called nucleotides were treated as a match to all four nucleotides if there was no mismatch; otherwise, they were treated as a mismatch. All nucleotides were included in the Hamming distance calculation at this step. To minimize misassignment, we constructed the codebook and lookup table before filtering, as eliminating a potential barcode early on may result in its axonal rolonies being assigned to another barcoded cell within the maximum Hamming distance.

Axonal barcode correction. During axonal base-calling, it was possible for a single axonal rolony in one sequencing cycle to link to more than one rolony in another sequencing cycle. This can result in (1) one rolony belonging to multiple different barcodes; (2) the same axonal rolony being called multiple times and linked to different rolonies in other cycles, but belonging to the same barcode. To address these issues, we took the following steps: (1) a rolony in a cycle linked to more than one barcode was excluded and the cycle was assigned as non-base-called; (2) barcodes that did not meet the requirements for length and interval were excluded; (3) barcodes with similar sets of rolonies were condensed into the one with the most base-called digits.

The Hamming distance between a pair of barcodes was calculated as the total number of mismatches between them. By default, non-base-called nucleotides were treated as a match to all four nucleotides. In this SINV library, the 9th and 10th nucleotides were fixed and, therefore, excluded from the Hamming distance calculation, unless stated otherwise.

Soma identification. Soma barcode counts were determined by counting the number of pixels associated with a specific barcode at the injection site (AudI). However, these counts alone were not always reliable for identifying barcoded somata in our current setup,

potentially due to the following factors: (1) some somata were cut and split into two neighboring sections during sectioning; (2) loss of surface area of the section during sample preparation (e.g. due to over-digestion by pepsin); (3) weak signals in deep areas of the section due to insufficient permeabilization during sample preparation; (4) low soma barcode counts in some cells; (5) base-called areas appearing smaller than they should be due to alignment, stitching errors, and phasing; (6) soma base-calling being sensitive enough to identify dendritic, and occasionally axonal, rolonies in AudI.

To identify valid soma locations, we identified the brain section with the highest sum intensity of soma pixels as the soma section, and within this section, we identified the XY coordinates of the brightest pixels as soma locations. A soma needed at least 80 counts of its barcode within 100 μm of its location. Barcodes that did not meet these criteria were identified as barcodes without soma locations. In the registered data, the median distance between somata and the injection center is 267 μm.

Barcode filters
Filtering out error-prone barcodes. To reduce the number of non-specific barcodes, we applied the following filters: (1) barcodes with >6 continuous identical nucleotides were excluded (152 out of 13,919); (2) to minimize sequencing errors arising from bleedthrough during imaging, barcodes with more than 14-nt in Ch1/2 or Ch3/4 were excluded due to the similarity of excitation wavelengths (127 out of 13,767); (3) barcodes with more rolonies with 1 or 2 mismatches compared to no mismatches were excluded (82 out of 13,640). Non-base-called nucleotides were treated as a match to all four nucleotides at this step. Only barcodes that passed the count filter (1) with ≥10 rolonies in at least one target region, (2) with ≤1000 and ≥ 3 axonal barcode counts, and (3) with ≤ 7000 somal barcode counts were included for analysis (9185 out of 13,558 were included).

Secondary infection exclusion. We observed secondary infection in target brain regions, and most of the infected cells had a glial morphology. We manually identified 17 barcodes from these cells in all regions except AudI. Barcodes within a 4-Hamming distance of these identified barcodes were excluded from the analysis (92 out of 9185).

Repeated rolony exclusion. To avoid double-counting, we excluded repeated rolonies in overlapping imaging fields, such as the cortex and striatum. Specifically, in these overlapping areas, we only included one copy per barcode from different fields (exclusion range <25 μm).

Floating rolonies identification and exclusion. We observed that rolonies could sometimes float out of the soma and settle within a surrounding area. Among barcodes without a soma location, we also observed this floating rolony effect. Since the soma locations were unknown, we could not use the soma section to exclude these floating rolonies. Therefore, we used an alternative method to identify sections with floating rolonies. We used two criteria for identifying these sections: (1) the slide (and sometimes its neighboring slide) was the only one with rolonies in specific areas, and (2) the rolonies on the slides were widely and sparsely distributed. To identify rolonies that meet criterion (1), we excluded rolonies with neighbors (<140 μm) in other sections (>1 section away). To test whether criterion (2) was met, we identified a section to have enough rolonies that were far apart (≥3 rolonies/clusters with a distance beyond 50 μm). For barcodes with more than one such section, we selected the one with the widest rolony coverage. We used AudI, Thal, and Vis to find slides with floating rolonies.

We used this algorithm to identify sections with floating rolonies in cells with and without soma locations. Verification using cells with soma locations showed that the algorithm identified floating rolonies in 37.1% of cells. Within these positive barcodes, the algorithm had an

accuracy of 94.8% for identifying the range of sections for the soma (± 1 section). For cells without soma locations, the algorithm detected floating rolonies in 14.9% of barcodes. We manually validated 75 positive barcodes and found a false positive rate of 22.7%. We achieved 100% accuracy for identifying the range of sections for floating rolonies. False positives would result in the exclusion of true rolonies in a 40–60 μm area in selective targets, but since projections usually extend more than 200 μm, this had a limited effect on downstream analysis.

To exclude floating rolonies, we excluded axonal rolonies in AudI, Thal, and Vis from 2-3 sections around the soma sections for barcodes with soma locations, and from the floating rolony section for barcodes without soma locations. After applying these exclusions, 8,838 barcodes passed the count filters.

Non-neural cell exclusion. Although the strain of SINV we used preferentially infects neurons versus non-neuronal cells, this preference is not complete, so some non-neuronal cells are also infected. In this study we did not distinguish between neuronal and non-neuronal cells using cell-specific markers. To exclude non-neural cells from our analysis, we applied distance and counts criteria. Specifically, cells needed to have ≥3 axonal rolonies ≥200 μm from the soma or center of axonal rolonies in AudI, and 50 cells were excluded using this criterion. This criterion was applied because non-neural cells typically do not have long projections. It is worth noting that this process may also filter out neurons with short local projections.

Additional filtering after CCF registration. After registering the data to the CCFv3 reference frames we applied the following additional filters. We first deleted rolonies outside the CCFv3 brain area and performed additional floating rolony elimination in the hippocampus, ventricle and fimbria of CCFv3. Next, we set a minimum rolony counts for five major targets: 5 for the ipsilateral/contralateral cortex and thalamus, 3 for the striatum and midbrain. After filtering, we excluded 167 barcoded cells with <10 counts in any imaging region, as well as 16 non-neural cells. It is worth noting that these steps are optional and can be skipped. After the above-mentioned steps, we identified 8620 barcodes, including 3700 with soma location. Four barcodes had single-digit non-base-called nucleotides.

Manual assessment of base-calling results. To assess the sensitivity and accuracy of our automated base-calling pipeline, we compared it to manual base-calling. To evaluate the sensitivity of axonal rolony base-calling, we calculated the percentage of base-called rolonies in 17 randomly selected Seq14 images from target areas (3-6 ROIs per image, 300 × 300 pixels). Sensitivity was 44.5% ± 9%. To estimate the accuracy of axonal rolony base-calling, we randomly selected 18 barcodes and found that 0 out of 60 (0%) rolonies had >2 nt disagreements between the codebook and evaluator.

To evaluate the efficiency of soma base-calling, we manually selected 50–112 somata per image in 7 randomly selected sequencing images, and found that 63.9% ± 7.6% of somata were base-called. To estimate the accuracy of soma base-calling, we randomly selected 40 barcoded somata and manually base-called them, and found that 5 (12.5%) had >2 nt disagreements between the codebook and evaluator. To evaluate the accuracy of soma location, we randomly selected 90 barcoded somata and found that 79 (87.8%) were in agreement with the evaluator's assessment. It is worth noting that there was high signal density near the injection site, which may have contributed to some uncertainty in the evaluator's assessments.

Registering to Allen mouse brain CCFv3. To align the 3D data volume with the CCFv3[30], we used a manual linear registration process. We then applied nonlinear adjustments to the coronal plates using control point pairs, similar to the method used for image registration to the

brain volume. We used the Nissl reference map for this process. All reference maps used in this study (Nissl, average template, and annotation map) had a voxel resolution of 25 μm.

Evaluation of CCFv3-registration. To evaluate the accuracy of CCFv3-registration, we used a manual selection-based approach instead of intensity-based algorithms to minimize the impact from staining variabilities and uneven illumination. The edges of specific brain regions were manually selected on registered images and compared to their corresponding boundaries in CCFv3 (Supplementary Fig. 4D). To avoid bias, images and hemispheres were randomly chosen during the selection process. vGlut2 images (25 μm/voxel) were utilized to visualize the boundaries of brain regions. Six edges were chosen, including the outer edge of isocortex, outer edges of midbrain/thalamus/hypothalamus, outer edges of hippocampal formation (excluding entorhinal area), fasciculus retroflexus, mammillary related areas, and lateral edges of striatum/amygdala. The median shortest distance between the manually selected edge and the corresponding area boundary in CCFv3 was calculated.

The lateral edges of the registered striatum exhibited a lateral shift compared to CCFv3 and this discrepancy potentially led to errors in assigning striatal rolonies to lower layers of the cortex. To assess the impact of this issue, we manually annotated the ipsilateral striatum using vGlut2 registered images. Among the 6878 LatI-projecting cells, a total of 454 cells had striatal rolonies assigned to LatI, with 5.01 ± 5.35% (mean ± SD) of the rolony per cell. This analysis suggests that the influence on the assessment of cortical rolonies distribution in this paper was minimal.

Cortical flatmap and ML/AP/depth-coordinates. To compare projections across cortical regions and hemispheres, we generated a lookup table for a cortical flatmap from the CCFv3[30] (Supplementary Fig. 4E–J). The concept of this flatmap is similar to that of Wang et al.[30], but with some differences. The flatmap coordinates consisted of three axes, with one axis oriented in the same direction as the cortical columns and the other two on a plate perpendicular to the columns. We defined the outer and inner cortical boundaries using the outer boundaries of layers 1 and 6, respectively. To determine the direction of the cortical columns, we calculated the lines from each outer boundary voxel to the closest inner boundary voxel. The depth percentage was the percentage of cortical depth along individual column lines. Due to cortical curvature, the distance between two column lines may vary at different depths (i.e., the distance is larger in upper layers compared to lower layers). We chose the mid-cortical plate (~50% depth) as the reference plate for the other two axes. The values of the other two axes were calculated as the cumulative sum of voxel-to-voxel distances on the plate, and column lines were assigned to the values of their intersections at the reference plate. To obtain continuous, smooth values in all three axes, we applied an average filter.

Following general practice, we divided the reference plate into medial-lateral (ML) and anterior-posterior (AP) axes. Our goal in creating the flatmap was to simply flatten the cortex for physical distance, rather than attempting to represent biological gradients. We determined the definition of each axis with the following considerations: (1) rotating the brain around the x-axis in 3D space changes the direction and voxel value of the AP-axis; (2) similar to earth mapping, it is impossible to get a flat and continuous cortical plate without distorting the direction of the axes or the point-to-point distance due to cortical curvature. Although the midline is generally considered the 'medial' part of the brain, we found that setting the midline as a fixed value to flatten the cortex with this algorithm caused relatively more distortion near the lateral region. Therefore, we used principal component analysis (PCA) on the reference plate of the right hemisphere to define the 1st axis as AP and the 2nd axis as ML, and verified this visually. The contour line of the median AP and ML values was used as

the reference line for flattening. The AP value was assigned as the distance to the AP reference line on the reference plate, and the ML value was assigned as the distance to the ML reference line with the minimum AP value change along the reference plate. The minimum value in both axes per hemisphere was set to 1. This flattening method was unable to differentiate between cortical regions folded towards the midline and the increased distortion at the lateral edge. However, since these were not the target areas of this dataset, the flatmap algorithm did not adjust for them. Additionally, this flatmap preserved the subtle voxel difference between the left and right hemispheres in CCFv3.

We used these lookup tables with interpolation to convert the registered rolony and soma locations into ML/AP/depth coordinates. To minimize interpolation error near the edges, we applied a 50 μm non-zero average filter to the outer edge of the cortex. For visualization purposes, we assigned the ML-values of the left cortex as negative and the right cortex as positive, and excluded the range of the AP-axis without cortical rolonies. During this process, two of the 3700 somata were excluded, resulting in a total of 3698 somata.

After registration, we defined the areas of four major projection targets (cortex, thalamus, striatum, and midbrain) using the CCFv3. We further divided the cortex into ipsilateral and contralateral cortices using the midline (Supplementary Fig. 6A). We drew the brain boundaries based on the parents of the 11th level of CCFv3. In the cortical flatmap, we represented the area boundaries by boundaries between 45–55% cortical depth, unless specified otherwise.

Cortical layer gradience
In addition to utilizing cortical layers as anatomical markers, we computed gradients within each layer to detect potential biological variations. Cortical layer positions were determined using the Allen CCFv3 at a voxel resolution of 25 μm. The cortex data was then transformed into flatmap coordinates, and gradients within each layer were calculated for every ML-AP position along the cortical depth.

Simulated retrograde tracing
We manually identified three injection centers for simulated retrograde tracing on the flatmap. We defined a range of 300 μm around the center as the injection/patch region. To be considered positive for retrograde tracing, a cell must meet the following criteria: (1) be from the IT class, (2) have ≥ 10 rolonies within the patch region, and (3) have a soma location. To identify cells that specifically project to a contralateral patch, the patch/CtxC rolony count ratio must be ≥ 75%.

Single-cell tracing reconstruction
We created reconstructions by connecting the registered xyz-coordinates of rolonies and soma from the same barcoded cells. We first connected data points (including rolonies and soma) to their closest neighbor to form clusters, then connected each cluster to the nearest cluster via the closest data points until all clusters were connected. We set the maximum distance for connecting two data points at 1000 μm. We only included cells with soma location in the reconstruction, and dilated the somata for visualization purposes.

We computed the transparent outline of the brain using the CCFv3 annotation map. In coronal view images, we excluded stacks anterior or posterior to the current dataset (e.g., olfactory bulb and cerebellum) for visualization purposes.

Grouping major cell types
We divided barcoded neurons into CF and IT cells based on projections to the ipsilateral thalamus and superior colliculus. CF cells had projections to either the Thal or SupCol (Fig. 3A) with minimum rolony counts as described above; all other cells were assigned as IT cells.

We used a two-step approach to classify Thal+ cells as either ET or CT cells. In the first step, we grouped cells based on the presence of

rolonies in the striatal-thalamic fiber and thalamic reticular nucleus. The AUD axons in this region could be divided into two bundles, a dorsal and a ventral bundle in the coronal view and corresponding to axons from CT and ET cells[28]. We manually defined a region of interest in this region using registered xyz-coordinates (x: 8250–9000 μm; y: 3500–5000 μm; z: 6750–7500 μm; red region in Supplementary Fig. 7C) and divided the rolonies within it into two groups based on their y-axis location: the top half were classified as CT cells and the bottom half were classified as ET cells. We then assigned each individual rolony to the most frequent group of its nearest 10 neighbors and followed this by assigning each barcoded cell to the most frequent group. This process was repeated until convergence or after 100 iterations. The cell type for each barcoded cell was represented by the most frequent group of rolonies within the region of interest. The results of this initial grouping are shown in Supplementary Fig. 7D (930 of 1134 Thal+ cells were assigned to the CT/ET group; CT: 581; ET: 349). In the second step, we assigned all thalamic rolonies to the most frequent group of their nearest 10 neighbors, and the cell type for each barcoded cell was represented by the most frequent group of thalamic rolonies. 58 of the 930 cells were assigned to a different group in this step compared to the first step. The final results of the ET/CT grouping are shown in Supplementary Fig. 7E (CT: 713; ET: 421). Overall, this approach was able to classify the cell types for 91.2% (321/352) of Thal+ cells that project to the thalamus and the superior colliculus as ET cells and 8.8% (31) as CT cells, indicating that axonal BARseq can effectively identify cell types. We also observed that CT cells have rolonies in the striatum due to their axons traveling through the region to reach the thalamus. Visual examination showed that the majority of cells with rolonies in the striatum belong to the ET group (Supplementary Fig. 7F).

IT cells were divided into two subtypes: ITi and ITc. IT cells with ≥ 5 rolonies in the contralateral cortex were assigned to the ITc group, while the rest were assigned to the ITi group.

Visualization and quantification of soma laminar distribution
To visualize the distribution of somata across groups, we plotted them using flatmap coordinates: x-axis, ML; y-axis, depth %. The plotting sequences were randomly shuffled across groups. Note that the ratio of the x-axis to the y-axis is not equal for visualization purposes.

To quantify the proportion of somata from different groups at different depths, we binned the soma depths into 5% bins and calculated the percentages for each bin: (group count) / (all group counts) × 100%.

Visualization and quantification of rolony laminar distribution
To visualize the rolonies in the CCFv3, we plotted them in registered xyz-coordinates using a coronal view. The brain outline was shown in gray.

To visualize the laminar distribution in the cortex, we presented the data as heatmaps, unless otherwise specified. The frequency of rolony depth within a region was determined for each cell or bin, utilizing bin sizes corresponding to either 1% or 5% of the depth, or fractions of 1/2 or 1/4 of the layers. The darkness of the grid represented the relative probability.

Cortical rolony analysis
In our experiments, we excluded cortical rolonies that were deeper than 95% due to their proximity to the fiber tract and potential registration errors. Most infected somata were localized to the middle layers. We excluded rolonies near the somata based on their xyz-coordinates, which may create uniform exclusion across cortical depth. Thus, for the cortical analysis (Figs. 4–5, Supplementary Fig. 8–11), we excluded rolonies that were located <95 percentile of the injection center on the ML-AP plate (indicated by the black disk; the injection center is the median soma location). As a control for this

exclusion, we also excluded rolonies in the same region on the other hemisphere (referred to as the LatC local-exclusion control).

Although the carrier protein VAMP2nλ was based on VAMP2, which localizes presynaptically, we found barcodes in dendrites as well. We excluded rolonies close to the somata using two filters as described above, so we believe the impact of dendritic barcodes on the cortical analysis is minimal.

The separation of Med and Lat targets was described in Fig. 4A, and we required a minimum of 5 rolonies per target for LatI/MedI/MedC/LatC-projection unless stated otherwise.

To calculate the normalized density of projections across cortical layers, we determined the thickness of each layer or bin. Bin thicknesses were computed using the cortical flatmap, excluding depths exceeding 95% as previously described. As the thickness of layers can vary across different cortical areas, we performed these calculations separately for the four cortical areas. The boundaries of each area were defined based on the locations of 95% of the rolonies within that area.

Cortical quantification of auditory GFP bulk tracing

The registered GFP bulk tracing data was downloaded from the Allen Mouse Brain Connectivity Atlas[6], with a voxel resolution of 25 μm. The cortical data were first transformed into flatmap coordinates. Within the ipsilateral lateral area, we excluded saturated pixels and their adjacent regions up to 187.5 μm, similar to the local rolony exclusion method described earlier. Thresholding and morphological reconstruction were applied to remove autofluorescence backgrounds, including those from blood vessels. Additionally, we excluded the outer cortical edges of the flattened data (up to 212.5 μm on the cortical plate) due to distortions that occurred during the flattening process. To maintain consistency for comparative analysis, we also excluded regions extending beyond our dataset along the AP-axis. The criteria for defining medial and lateral areas are as shown in Fig. 4A. Furthermore, for consistency, we employed the same normalization factor (layer thickness) for normalized density as was used in the rolony analysis mentioned above.

To assess the differences in laminar projections within the samples from the Allen dataset, as well as between the Allen dataset and our current axonal BARseq dataset, we performed the two-sample Kolmogorov–Smirnov test (Supplementary Fig. 8C). In brief, the frequency distributions of projections along the cortical depth (Supplementary Fig. 8B) were transformed into cumulative distributions. We then calculated the Kolmogorov–Smirnov distances (KS-distances), using the maximum absolute difference between the two cumulative distributions. For comparisons within the Allen dataset (Allen vs. Allen), all-to-all comparisons were conducted for each cortical area, and the average KS-distance for each experiment was used to represent the differences within the dataset. For the comparisons between the Allen dataset and axonal BARseq data (Allen vs. axonal BARseq), we compared the bulk projections of rolonies (Fig. 4B) against individual experiments from the Allen dataset.

Lat-projecting IT cell grouping

We selected Lat-projecting IT cells with a minimum of 5 rolonies in LatI/C and divided them into three groups based on soma layer (Fig. 5A). However, not all the barcoded cells have a known soma location (as described above), so we only included Lat-projecting cells with a known soma location in the analysis. As a control, we grouped barcoded cells without soma information into two groups based on projection depth, as shown in Supplementary Fig. 9G–I, M, N.

Focal projection distance

For each barcoded cell, we calculated the all-to-all distances of the LatI/C rolonies on the ML-AP plate. For each rolony, we selected the shortest 33% of distances and used the mean of these distances to represent the 'focal projection distance' of the rolony. We then used the mean of the rolony focal projection distances to represent the distance for each cell.

We selected the shortest 33% distance as a measurement based on the following considerations: We wanted to capture the small range and tightness of the projection, so we calculated the focal projection distance using a subset of the nearest rolonies. We observed that cells can have more than one focal projection per target (e.g. the LatC projection from the orange cell in Fig. 5D), so we set a threshold (i.e. 33%) to exclude rolonies from other clusters. Based on our observations, most cells did not have many focal projections, and it was difficult to distinguish a cell with many focal projections from one with a sparse projection. Therefore, we assumed that cells have a maximum of three focal projections and calculated the distance from the closest 33% of rolonies.

To estimate the effect of rolony number on focal projection distance per cell, we randomly subsampled different numbers of rolonies from each barcoded cell and calculated the focal projection distance for each subsample. The ground truth distance was calculated using all rolonies from the same cell. We defined the sampling error as:

$$\mathrm{abs}(\mathrm{distance}_{sample} - \mathrm{distance}_{groundtruth})/\mathrm{distance}_{groundtruth} \times 100\%$$

We performed 100 random samplings per cell, and the median error represents the error per cell. The results are shown in Supplementary Fig. 9J. Thus, we only used cells with ≥55 Lat rolonies for the following analysis (Fig. 5I, Supplementary Fig. 9K–N).

Correlation between CT/CF fiber intensity and lower layer projection

Projections originating from deep-layer IT cells have been observed in the Allen Mouse Brain Connectivity Atlas[6], as indicated in Supplementary Fig. 10A. Given that injections in WT mice can infect various cell types across depths, it's important to estimate the proportion of infected deep-layer IT cells in individual experiments. Hence, we used CT/ET fiber intensity for estimation, based on the following considerations: when axons innervate a target, they often branch and establish multiple contacts, resulting in an increase in GFP intensity. However, this increase in GFP intensity might not be uniformly proportional across different cell types, injection sites, and animals. To minimize the influence of these variabilities, we chose to utilize the intensity of fibers before their innervation of subcortical targets. Furthermore, in this analysis, we assumed that the distribution of infected cells follows a unimodal pattern in the majority of experiments. This distribution comprises (1) layer 5 and above, (2) layers 5-6 and above, (3) layer 6.

We manually examined the fiber locations across 160 WT mice from the Allen Mouse Brain Connectivity Atlas. During this process, certain cortical regions were excluded primarily due to the following reasons: (1) CF routes entering the thalamus from the ventral side and dividing into smaller bundles to pass through the internal capsule (i.e., SSp-m, VISC). (2) The CT and ET routes follow trajectories at angles that make their separation challenging when observed on a coronal plane (i.e., ACA, ORB). (3) A combination of these two conditions. Considering these factors, the validation process for the separation of CT/ET fiber bundles was conducted in the RSP, SSp-bfd/tr, AUD, and VIS areas.

In these regions, the dorsal and ventral routes of projections consistently aligned with the CT and ET fibers, as indicated in Supplementary Fig. 10B. To compare the intensity of the CT and ET fibers, we utilized the representation of the dorsal and ventral routes. The intensities of these two routes were quantified by manually drawing lines across the route on the stacks with the highest intensity. For each fiber, three lines were drawn, and the resulting mean intensity was calculated to represent the fiber's intensity. To minimize the impact of saturation on measurements, we excluded mice with an injection

volume exceeding 0.2 mm³. Additionally, to minimize potential bias, the evaluator was blinded to the cortical projection patterns. Mice with fiber bundles that were difficult to differentiate were excluded.

To maintain consistency with Fig. 5 and to minimize the effects of traveling fibers and intensity saturation near the injection site, we focused on measuring homotopic callosal projections. This approach involved manually defining a rectangular region of interest on the projection cluster situated closest to the mirror injection site on the flattened data of each experiment. However, this approach does introduce a potential concern that certain callosal projections may not terminate symmetrically in the contralateral area. For instance, callosal projections originating from the primary VIS cortex might not terminate in the contralateral primary VIS; they could be more likely to terminate at the boundaries of the primary VIS[36]. To address this issue, we employed correlation analysis to filter out experiments lacking strong symmetric projection within the region of interest (Spearman's rho <0.5, along with manual confirmation). Additionally, samples with weak symmetric projections or injection sites positioned close to the flatmap's edge were excluded from the analysis. The flattened cortical data were obtained as described above in the auditory GFP bulk tracing analysis. Because the regions of interest were selected manually, we did not include AP-axis data exclusion and autofluorescent background exclusion in this analysis. The normalized density was calculated using the layer thickness within the region of interest.

Software and statistical analysis
We used MATLAB (2021a), ImageJ/FIJI, and MIJ[37] for data processing and visualization. We used MATLAB and GraphPad Prism 9/10 for statistical analyses, as indicated in the text. **p-value < 0.01, ***p-value < 0.001, ****p-value < 0.0001, unless stated otherwise.

To estimate confidence intervals (2.5 and 97.5%), bootstrapping was performed for each group (2000 iterations). * indicates that the confidence intervals of two groups have no overlap.

The data distributions presented in Figs. 4–5 and Supplementary Figs. 8-9 are detailed in SupTable 5.

Reporting summary
Further information on research design is available in the Nature Portfolio Reporting Summary linked to this article.

Data availability
The raw and processed BARseq data generated in this study have been deposited in the Brain Image Library[38] under BIL uuid, dfabd518f37ff2e5. Source data are provided as a Source Data file. Source data are provided with this paper.

Code availability
Code for image processing and analysis is available on GitHub (https://github.com/ZadorLaboratory/axonalBARseq).

References
1. Herculano-Houzel, S., Mota, B. & Lent, R. Cellular scaling rules for rodent brains. *Proc. Natl Acad. Sci. USA.* **103**, 12138–12143 (2006).
2. Winnubst, J. et al. Reconstruction of 1,000 Projection Neurons Reveals New Cell Types and Organization of Long-Range Connectivity in the Mouse Brain. *Cell* **179**, 268–281.e13 (2019).
3. Peng, H. et al. Morphological diversity of single neurons in molecularly defined cell types. *Nature* **598**, 174–181 (2021).
4. Gao, L. et al. Single-neuron projectome of mouse prefrontal cortex. *Nat. Neurosci.* **25**, 515–529 (2022).
5. Qiu, S. et al. Whole-brain spatial organization of hippocampal single-neuron projectomes. *Science* **383**, eadj9198 (2024).
6. Oh, S. W. et al. A mesoscale connectome of the mouse brain. *Nature* **508**, 207–214 (2014).
7. Harris, J. A. et al. Hierarchical organization of cortical and thalamic connectivity. *Nature* **575**, 195–202 (2019).
8. Muñoz-Castañeda, R. et al. Cellular anatomy of the mouse primary motor cortex. *Nature* **598**, 159–166 (2021).
9. Kebschull, J. M. et al. High-Throughput Mapping of Single-Neuron Projections by Sequencing of Barcoded RNA. *Neuron* **91**, 975–987 (2016).
10. Huang, L. et al. BRICseq Bridges Brain-wide Interregional Connectivity to Neural Activity and Gene Expression in Single Animals. *Cell* **183**, 2040 (2020).
11. Chen, Y. et al. High-throughput sequencing of single neuron projections reveals spatial organization in the olfactory cortex. *Cell* **185**, 4117–4134.e28 (2022).
12. Chen, X. et al. High-Throughput Mapping of Long-Range Neuronal Projection Using In Situ Sequencing. *Cell* **179**, 772–786.e19 (2019).
13. Sun, Y.-C. et al. Integrating barcoded neuroanatomy with spatial transcriptional profiling enables identification of gene correlates of projections. *Nat. Neurosci.* **24**, 873–885 (2021).
14. Zeisler, Z. R. et al. High-throughput sequencing of macaque basolateral amygdala projections reveals dissociable connectional motifs with frontal cortex. *bioRxiv* 2023.01.18.524407 https://doi.org/10.1101/2023.01.18.524407 (2023).
15. Hausmann, F. S., Barrett, J. M., Martin, M. E., Zhan, H. & Shepherd, G. M. G. Axonal Barcode Analysis of Pyramidal Tract Projections from Mouse Forelimb M1 and M2. *J. Neurosci.* **42**, 7733–7743 (2022).
16. Tsoi, S. Y. et al. Telencephalic outputs from the medial entorhinal cortex are copied directly to the hippocampus. *Elife* **11**, e73162 (2022).
17. Webb, J. M., Ma, M., Yin, C., Ptáček, L. J. & Fu, Y.-H. An excitatory peri-tegmental reticular nucleus circuit for wake maintenance. *Proc. Natl. Acad. Sci.* **119**, e2203266119 (2022).
18. Klingler, E. et al. Temporal controls over inter-areal cortical projection neuron fate diversity. *Nature* **599**, 453–457 (2021).
19. Mathis, V. P., Williams, M., Fillinger, C. & Kenny, P. J. Networks of habenula-projecting cortical neurons regulate cocaine seeking. *Sci. Adv.* **7**, eabj2225 (2021).
20. Gergues, M. M. et al. Circuit and molecular architecture of a ventral hippocampal network. *Nat. Neurosci.* **23**, 1444–1452 (2020).
21. Han, Y. et al. The logic of single-cell projections from visual cortex. *Nature* **556**, 51–56 (2018).
22. Chen, X., Sun, Y.-C., Church, G. M., Lee, J. H. & Zador, A. M. Efficient in situ barcode sequencing using padlock probe-based BaristaSeq. *Nucleic Acids Res.* **46**, e22–e22 (2018).
23. Harris, K. D. & Shepherd, G. M. G. The neocortical circuit: themes and variations. *Nat. Neurosci.* **18**, 170–181 (2015).
24. Tasic, B. et al. Adult mouse cortical cell taxonomy revealed by single cell transcriptomics. *Nat. Neurosci.* **19**, 335–346 (2016).
25. Tasic, B. et al. Shared and distinct transcriptomic cell types across neocortical areas. *Nature* **563**, 72–78 (2018).
26. Cai, D. et al. Distinct Anatomical Connectivity Patterns Differentiate Subdivisions of the Nonlemniscal Auditory Thalamus in Mice. *Cereb. Cortex* **29**, 2437–2454 (2019).
27. Llano, D. A. & Sherman, S. M. Evidence for nonreciprocal organization of the mouse auditory thalamocortical-corticothalamic projection systems. *J. Comp. Neurol.* **507**, 1209–1227 (2008).
28. Mitrofanis, J. & Baker, G. E. Development of the thalamic reticular and perireticular nuclei in rats and their relationship to the course of growing corticofugal and corticopetal axons. *J. Comp. Neurol.* **338**, 575–587 (1993).
29. Lyamzin, D. & Benucci, A. The mouse posterior parietal cortex: Anatomy and functions. *Neurosci. Res.* **140**, 14–22 (2019).
30. Wang, Q. et al. The Allen Mouse Brain Common Coordinate Framework: A 3D Reference Atlas. *Cell* **181**, 936–953.e20 (2020).
31. Egger, R. et al. Cortical Output Is Gated by Horizontally Projecting Neurons in the Deep Layers. *Neuron* **105**, 122–137.e8 (2020).

32. Livet, J. et al. Transgenic strategies for combinatorial expression of fluorescent proteins in the nervous system. *Nature* **450**, 56–62 (2007).

33. Kebschull, J. M., Garcia da Silva, P. & Zador, A. M. A New Defective Helper RNA to Produce Recombinant Sindbis Virus that Infects Neurons but does not Propagate. *Front. Neuroanat.* **10**, 56 (2016).

34. Joffroy, B., Uca, Y. O., Prešern, D., Doye, J. P. K. & Schmidt, T. L. Rolling circle amplification shows a sinusoidal template length-dependent amplification bias. *Nucleic Acids Res* **46**, 538–545 (2018).

35. Edelstein, A., Amodaj, N., Hoover, K., Vale, R. & Stuurman, N. Computer control of microscopes using µManager. *Curr. Protoc. Mol. Biol.* **Chapter 14**, Unit14.20 (2010).

36. Wang, Q., Gao, E. & Burkhalter, A. Gateways of Ventral and Dorsal Streams in Mouse Visual Cortex. *J. Neurosci.* **31**, 1905–1918 (2011).

37. Sage, D., Prodanov, D., Tinevez, J.-Y. & Schindelin, J. MIJ: Making Interoperability Between ImageJ and Matlab Possible. http://bigwww.epfl.ch/sage/soft/mij/Poster-MIJ-Daniel-Sage.pdf (2012).

38. Benninger, K. et al. Cyberinfrastructure of a Multi-Petabyte Microscopy Resource for Neuroscience Research. in *Practice and Experience in Advanced Research Computing* 1–7 (Association for Computing Machinery, New York, NY, USA, 2020).

Author contributions

L.Y., X.C., and A.M.Z. conceived the study. L.Y. performed experiments and data analysis. H. Z. and G. L. H. developed the VAMP2nλ vector. L.Y. and A.M.Z. wrote the paper.

Competing interests

A.M.Z. is a founder and equity owner of Cajal Neuroscience and a member of its scientific advisory board. The remaining authors declare no competing interests.

Additional information

Supplementary information The online version contains supplementary material available at https://doi.org/10.1038/s41467-024-52756-x.

Correspondence and requests for materials should be addressed to Anthony M. Zador.

Peer review information *Nature Communications* thanks the anonymous reviewers for their contribution to the peer review of this work. A peer review file is available.

Reprints and permissions information is available at http://www.nature.com/reprints

Publisher's note Springer Nature remains neutral with regard to jurisdictional claims in published maps and institutional affiliations.